Report

Cell Reports

EphrinB2 and GRIP1 stabilize mushroom spines during denervation-induced homeostatic plasticity

Graphical abstract

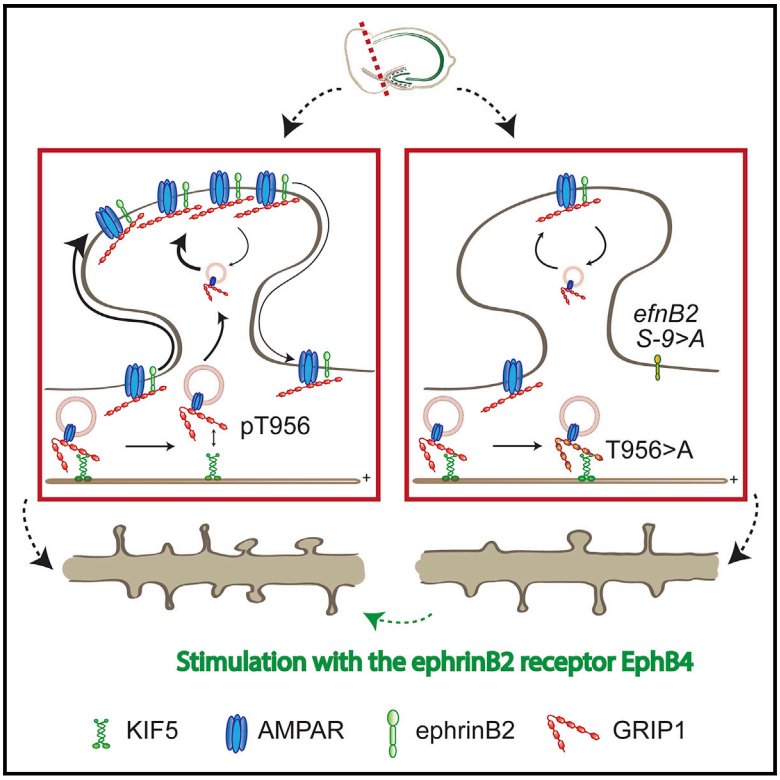

Authors

Diane Bissen, Maximilian Ken Kracht, Franziska Foss, Jan Hofmann, Amparo Acker-Palmer

Correspondence

acker-palmer@bio.uni-frankfurt.de

In brief

The physiological and morphological correlates of homeostatic plasticity after lesion are still unclear. Bissen et al. show that lesion-induced input loss predominantly affects mushroom spines and induces a homeostatic AMPAR redistribution to the surface, thus promoting mushroom spine stabilization and their recovery. These mechanisms are mediated by GRIP1 and ephrinB2.

Highlights

- Denervation induces mushroom spine loss and AMPAR redistribution to the surface
- GRIP1 and ephrinB2 mediate homeostatic mechanisms after lesion
- Stimulation with the ephrinB2 receptor EphB4 promotes a surface shift of AMPARs
- AMPARs surface shift restores impaired spine recovery after lesion in GRIP1 mutants

Bissen et al., 2021, Cell Reports *34*, 108923
March 30, 2021
https://doi.org/10.1016/j.celrep.2021.108923

CellPress

Cell Reports

CellPress
OPEN ACCESS

Report

EphrinB2 and GRIP1 stabilize mushroom spines during denervation-induced homeostatic plasticity

Diane Bissen,[1,2] Maximilian Ken Kracht,[1] Franziska Foss,[1] Jan Hofmann,[1] and Amparo Acker-Palmer[1,2,3,4,*]
[1]Institute of Cell Biology and Neuroscience and Buchmann Institute for Molecular Life Sciences (BMLS), University of Frankfurt, Max-von-Laue-Str. 15, 60438 Frankfurt am Main, Germany
[2]Max Planck Institute for Brain Research, Max von Laue Str. 4, 60438 Frankfurt am Main, Germany
[3]Cardio-Pulmonary Institute (CPI), Max-von-Laue-Str. 15, 60438 Frankfurt am Main, Germany
[4]Lead contact
*Correspondence: acker-palmer@bio.uni-frankfurt.de
https://doi.org/10.1016/j.celrep.2021.108923

SUMMARY

Despite decades of work, much remains elusive about molecular events at the interplay between physiological and structural changes underlying neuronal plasticity. Here, we combined repetitive live imaging and expansion microscopy in organotypic brain slice cultures to quantitatively characterize the dynamic changes of the intracellular versus surface pools of GluA2-containing α-amino-3-hydroxy-5-methyl-4-isoxazolepropionic acid receptors (AMPARs) across the different dendritic spine types and the shaft during hippocampal homeostatic plasticity. Mechanistically, we identify ephrinB2 and glutamate receptor interacting protein (GRIP) 1 as mediating AMPAR relocation to the mushroom spine surface following lesion-induced denervation. Moreover, stimulation with the ephrinB2 specific receptor EphB4 not only prevents the lesion-induced disappearance of mushroom spines but is also sufficient to shift AMPARs to the surface and rescue spine recovery in a GRIP1 dominant-negative background. Thus, our results unravel a crucial role for ephrinB2 during homeostatic plasticity and identify a potential pharmacological target to improve dendritic spine plasticity upon injury.

INTRODUCTION

A core feature of neurons is their ability to adapt to changes (i.e., their plasticity). Hebbian and homeostatic forms of plasticity, which are, respectively, believed to underlie associative learning and support network stability, were traditionally considered as separate processes; recent evidence, however, suggests that homeostatic plasticity acts as a metaplasticity mechanism that integrates changes in neuronal activity and supports Hebbian learning (Arendt et al., 2013; Kirkwood et al., 1996, reviewed in Li et al., 2019). Identifying common molecular players involved in both forms of plasticity is therefore paramount to understanding how they crosstalk to achieve network function.

At excitatory synapses, dendritic spine size positively correlates with the number of α-amino-3-hydroxy-5-methyl-4-isoxazolepropionic acid receptors (AMPARs), and both parameters are correspondingly adjusted in response to plasticity-inducing stimuli, such as during the classical Hebbian paradigms of long-term potentiation (LTP) or depression (LTD) (Matsuzaki et al., 2004; Zhou et al., 2004, reviewed in Forrest et al., 2018). Ultimately, the number of receptors in the postsynaptic membrane (together with their physiological properties) is key to the reception of the information shared by the presynaptic neurons, and receptor trafficking between synaptic and non-synaptic pools is thus tightly controlled (Barberis, 2020; Henley and Wilkinson, 2016). In the case of AMPARs, a significant contingent of auxiliary proteins regulating their trafficking and their stabilization at the dendritic membrane have been identified. Among them is glutamate receptor interacting protein (GRIP1), a 7-PDZ domain-containing adaptor protein interacting, among others, with the GluA2 and GluA3 AMPAR subunits, with the class B of the Eph/ephrin family of signaling molecules, and with the motor protein KIF5, which directs GRIP1 and its various cargoes to the dendritic compartment (Dong et al., 1997; Setou et al., 2002; Torres et al., 1998, reviewed in Bissen et al. (2019). The latter is regulated by the phosphorylation of the threonine (T) 956 residue, upon which KIF5 is displaced and replaced by 14-3-3 proteins, leading to the release of the cargo; in the case of AMPARs, this is a crucial step for their availability for insertion at the dendritic membrane (Geiger et al., 2014). Moreover, ephrinB2 binding to GRIP1 promotes the activity-dependent insertion and stabilization of AMPARs at the dendritic surface via a complex that also includes the Reelin receptor ApoER2. The phosphorylation of a key residue of ephrinB2, the serine (S)-9, is necessary for the interaction between ephrinB2 and GRIP1 and the subsequent formation of the complex and AMPAR insertion (Essmann et al., 2008; Pfennig et al., 2017). Consistently, LTP, which depends on an increase in synaptic AMPARs, is reduced in mice, in which the complex formation is impaired (Pfennig et al., 2017). Recently, GRIP1 was shown to be required for synaptic upscaling, but not downscaling, with a primary role in supporting the surface pool of AMPARs (Gainey et al., 2015;

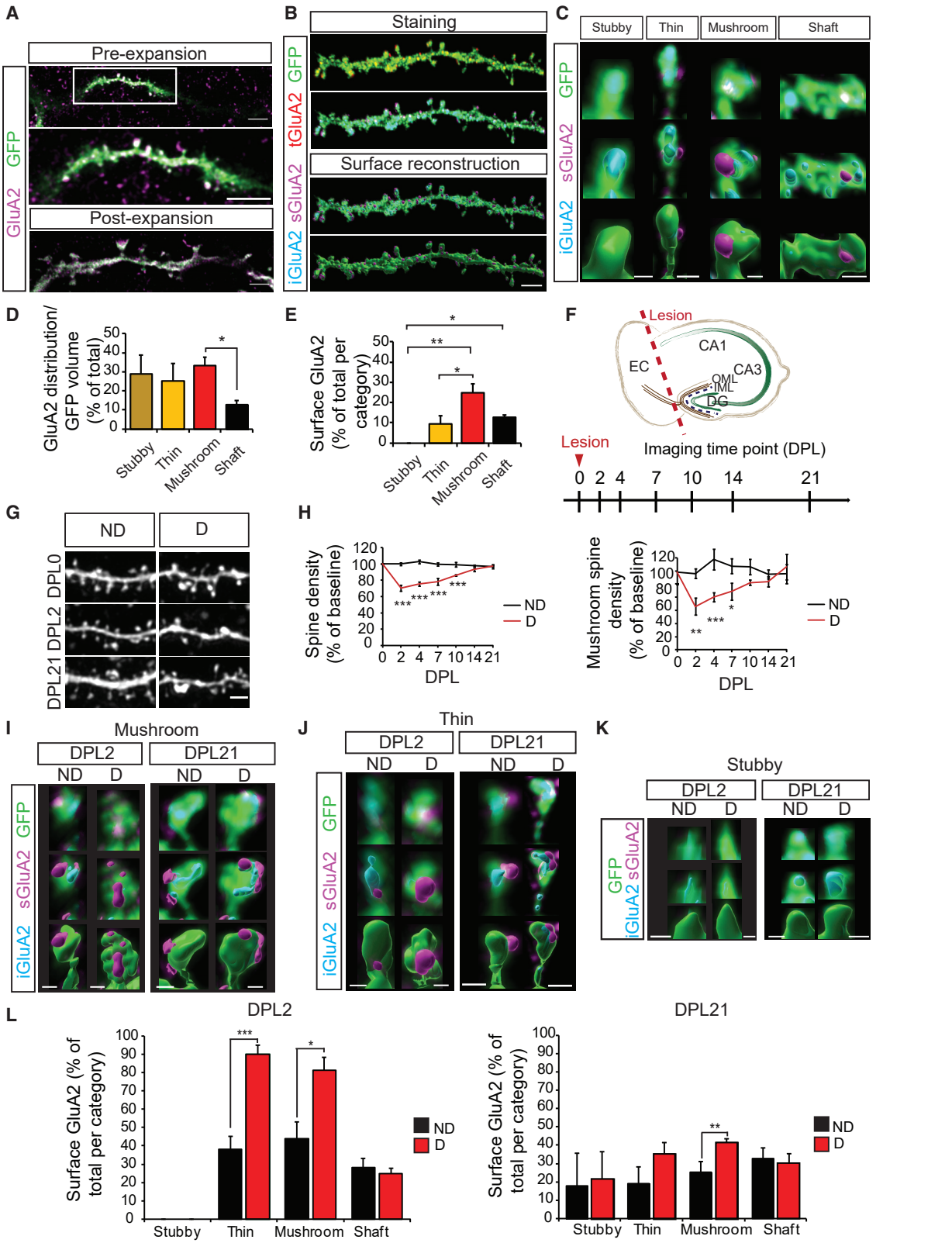

(legend on next page)

Tan et al., 2015). Whether GRIP1 is also involved in other forms of homeostatic plasticity and whether ephrinB2 also regulates the function of GRIP1 during homeostatic plasticity are currently unknown.

A deep understanding of AMPAR dynamics and its regulation is essential to our comprehension of synaptic function and plasticity. Intensive work, coupled with technical advancements in super-resolution imaging, has revealed new layers of complexity, such as the sub-synaptic organization of AMPARs in nanodomains (Ehlers et al., 2007; Kharazia and Weinberg, 1997; Scheefhals and MacGillavry, 2018). However, further research is required to deepen our understanding of the dynamic regulation of AMPAR movements in constitutive and plasticity-dependent contexts *in vivo*. Expansion microscopy is a recently developed technique enabling a significant enhancement in imaging resolution by physically increasing sample size (Chen et al., 2015). In this study, we applied this method to analyze the distribution of AMPARs in constitutive and plasticity-dependent conditions in organotypic slice cultures (OTCs) that can be used for the longitudinal assessment of changes over time ((Gähwiler, 1981); Humpel, 2015). Using this technique, we investigated the cellular and molecular events regulated by the cooperative action of ephrinB2 and GRIP1 during hippocampal homeostatic plasticity.

RESULTS

Denervation induces mushroom spine loss and AMPAR redistribution to the surface

We used entorhinal-hippocampal OTCs of mice expressing the enhanced green fluorescent protein (EGFP) under the Thy1 promoter (subsequently referred to as control mice) to visualize neuronal morphology in sparsely labeled principal cells in the hippocampus, and focused on granule cells in the dentate gyrus (DG) (Feng et al., 2000). After staining against GFP and the AMPAR subunit GluA2 in permeabilizing conditions, OTCs were submitted to expansion microscopy and were reliably magnified by a factor of 3–3.5× (Figure 1A). Following deconvolution (Huygens, SVI), the respective volumes of GFP and GluA2 staining in secondary dendrites of granule cells were reconstructed using Imaris (Bitplane), allowing the quantification of the distribution of GluA2-containing AMPARs along the dendritic stretch (Figure 1B). For further analysis, we subdivided the stretches in the shaft and spines; according to the classical paradigm, spines were visually classified as mushroom, thin, or stubby based on the respective size of their head and neck (Figures 1C and S1F–S1I) (Rochefort and Konnerth, 2012). The analysis of the amount of GluA2 reported to the GFP volume of the corresponding spine or shaft revealed that the proportion of spine volume occupied by GluA2 is remarkably similar between spine types (Figure 1D). Finally, the increased resolution given by expansion microscopy allowed us to discriminate between external GluA2 signal (defined as staining at the surface of the GFP signal) and internal GluA2 signal (defined as staining within the corresponding GFP signal). The validity of this proxy was confirmed by performing staining in non-permeabilizing and permeabilizing conditions followed by expansion microscopy in cultured hippocampal neurons (Figures S1B–S1E). We thus investigated the repartition of GluA2 between the surface and intracellular pools. Strikingly, GluA2-AMPARs were predominantly located within the neuron, indicating that the internal pool outnumbers surface receptors (Figure 1E). Moreover, consistent with the literature reporting stronger AMPAR currents in larger spines (Matsuzaki et al., 2001; Noguchi et al., 2011), we found on average the highest proportion of surface AMPARs in mushroom spines (Figure 1E). Intriguingly, most stubby spines only displayed internal GluA2, corroborating a modest role of these spines in neuronal connections. We performed the same analysis in secondary dendrites in the *stratum radiatum* of adult CA1 pyramidal cells and observed a remarkably similar distribution, suggesting that this pattern is not restricted to dentate granule cells (Figures S1J–S1L).

Figure 1. Lesion-induced spine loss and subsequent recovery are accompanied by AMPAR redistribution

(A) OTCs from GFP-expressing mice (green) and stained with antibodies against the GluA2 subunit of AMPARs (magenta). Representative image of a dendritic stretch pre- (top; center: higher magnification) and post- (bottom) expansion.

(B) Representative example of a stained dendritic stretch with the original GluA2 staining (red, tGluA2), the GluA2 staining subdivided between surface (magenta, sGluA2) and internal (cyan, iGluA2) pools based on the GFP reconstruction (top), and their surface reconstruction using Imaris (below). The pseudocolor convention remains the same throughout the article.

(C) Representative surface reconstructions of stubby, thin, and mushroom spines and shafts (bottom row). GluA2 and GFP staining are shown in the top row; GluA2 staining is displayed in 2 pseudocolors representing the 2 different pools (surface GluA2 [sGluA2] in magenta and internal GluA2 [iGluA2] in cyan) based on the GFP reconstruction. The surface reconstruction of the GFP staining has been omitted in the center row to enable visualization of the complete GluA2 reconstruction.

(D) Quantification of GluA2 distribution normalized to GFP volume, shown as percentage of total GluA2/GFP corresponding to (C); n = 5 neurons, 2 experiments.

(E) Quantification of surface GluA2, shown as percentage of total GluA2 per compartment corresponding to (C); n = 5 neurons, 2 experiments.

(F) Anatomy of an entorhinal-hippocampal organotypic slice culture showing the position of the lesion and timeline of imaging experiments. CA, *cornu ammonis*; DG, dentate gyrus; DPL, day post-lesion; EC, entorhinal cortex; IML, inner molecular layer; OML, outer molecular layer.

(G) Representative pictures of dendritic stretches of dentate granule cells in non-denervated and denervated OTCs. D, denervated; ND, non-denervated.

(H) Quantification of total spine (upper graph) and mushroom spine (lower graph) density as relative ratios to baseline (DPL0) corresponding to (G); n = 5–7 neurons per condition, 4 experiments.

(I–K) Representative surface reconstructions of mushroom (I), thin (J), and stubby (K) spines from non-denervated and denervated OTCs at DPL2 and DPL21.

(L) Quantification of surface GluA2 in D and ND OTCs, represented as percentage of total GluA2 in each compartment corresponding to (I)–(K); n = 5 neurons per condition, 2 experiments.

Scale bars: 5 μm (A top and bottom), 2 μm (A center, B, and G), 1 μm (C and I–K). Graphs show means ± SEMs. *p < 0.05; **p < 0.01; ***p < 0.001. Exact p values in Table S1.

See also Figures S1 and S2.

We then took advantage of the 3D structure and long life of OTCs and induced homeostatic plasticity by sectioning the perforant pathway from the entorhinal cortex projecting specifically to the outer molecular layer of the granule cells of the DG without affecting the inner layer (Figure 1F). Baseline spine density and morphology were similar in stretches subsequently selected for denervation or as controls (Figures S2A and S2B). Denervation triggered a reduction in spine density in the DG granule cells right after lesion (day post-lesion [DPL] 2), which slowly recovered to baseline levels within 3 weeks (DPL21) (Figures 1G and 1H, left), consistent with previous reports (Perederiy and Westbrook, 2013; Vlachos et al., 2012a). In addition, we further analyzed the specific effect of the lesion on mushroom, thin, and stubby spines and showed that mushroom spines were particularly affected (Figure 1H, right). Thin and stubby spines showed only a minimal loss after lesion, with no significant differences to the non-denervated OTCs (Figures S2C and S2D).

Lasting reduction in network activity triggers homeostatic synaptic strengthening by increasing the number of surface synaptic AMPARs (Turrigiano, 2017; Turrigiano et al., 1998). Moreover, denervation in OTCs leads to a rapid augmentation in AMPAR currents, with a fast return to baseline (Vlachos et al., 2012b). Therefore, we next assessed the effect of denervation on AMPAR distribution using expansion microscopy (Figures 1I–1L and S2). The total levels of GluA2/GFP volume did not significantly change across time in spines after the lesion (Figure S2E). However, the lesion induced a strong increase of surface GluA2 in thin and mushroom spines at DPL2, a change that was still present at DPL21, significantly for mushroom spines and with a trend for the thin spines (Figures 1I, 1J, and 1L).

GRIP1 is required for homeostatic plasticity-induced GluA2-containing AMPAR dynamics

The scaffold protein GRIP1 was shown to be involved in AMPAR delivery to the synapses (Hoogenraad et al., 2005), and we previously found that it is important for *de novo* surface insertion of AMPARs and for dendritic development, the latter through the phosphorylation of its T956 residue (Essmann et al., 2008; Geiger et al., 2014; Pfennig et al., 2017). To investigate the requirement of the T956 phosphorylation in GRIP1 for plasticity-induced AMPAR insertion, we used a transgenic mouse line expressing GRIP1 T956 > A transgene (*Grip1*-T956 > A), in which the threonine residue has been replaced by alanine. The GRIP1 T956 > A mutated protein acts as a dominant-negative over the endogenous GRIP1, and cargoes transported in the neuronal secretory pathway are trapped at the cytoskeleton, resulting in impaired dendritogenesis (Geiger et al., 2014). T956 phosphorylation was required for activity-induced new insertion of GluA2-containing AMPARs at the dendritic membrane as assessed using an AMPAR membrane insertion assay (Figures S3A and S3B). We then addressed the role of GRIP1 in denervation-induced homeostatic plasticity in OTCs from *Grip1*-T956 > A mice. Baseline total and mushroom spine density, as well as the total content and distribution of GluA2-containing AMPARs, were unaffected in *Grip1*-T956 > A mice, suggesting that the endogenous wild-type GRIP1 proteins are sufficient to support constitutive neuronal function (Figure S3C–S3E). However, GRIP1 T956 > A dominant-negative expression significantly impaired the previously observed spine density recovery after lesion in OTCs, which failed to return to baseline (compare Figures 2A–2C to Figure 1G and 1H). To correlate the inability of *Grip1*-T956 > A mutant OTCs to undergo recovery with a change in the dynamics of AMPAR at the mutant spines, we stained for GluA2 and performed expansion microscopy. Analysis of GluA2-containing AMPAR dynamics revealed that the denervation-induced shift of GluA2 toward the surface in thin and mushroom spines was severely impaired in the denervated *Grip1*-T956 > A OTCs (compare Figures 2D–2G to Figures 1I–1L). The GRIP1 T956 > A mutation even resulted in an acute reduction of surface GluA2 at the dendritic membrane that was significant for mushroom spines and shafts, indicating a strong dependency on GRIP1 to stabilize AMPARs at the surface (Figure 2G). As in the control situation, denervation did not significantly affect the total population of GluA2 in the different dendritic compartments, suggesting that GRIP1 primarily mediates plasticity-induced GluA2-containing AMPAR redistribution rather than its total content (Figure S3F).

GRIP1 function in homeostatic plasticity requires binding to ephrinB2

We have previously shown that GRIP1/ephrinB2 binding, the formation of the complex including GluA2, and the subsequent promotion of the surface pool of AMPARs depend on the phosphorylation of a serine residue (S-9) in the cytoplasmic tail of ephrinB2 (Essmann et al., 2008; Pfennig et al., 2017). Therefore, we next addressed the involvement of ephrinB2 by using a nervous system-specific null mutation for ephrinB2 (*Nes cre; efnB2*$^{lox/lox}$) and a knockin where the *efnB2* gene has been replaced by a point mutation in the S-9 to alanine (*efnB2 S-9 > A*). In both mouse lines, constitutive total and mushroom spine density is unaffected by the mutations (Figures S4B, S4C, S4E, and S4F). We lesioned OTCs from both mutants and their control littermates and followed longitudinally spine density after denervation. Spine density, and specifically mushroom spine density, recovered from lesion-induced loss in control littermates, but not in the ephrinB2 knockout OTCs (Figures S4A and S4D) nor in the ephrinB2 serine mutants (Figures 3A and 3B), suggesting that GRIP1 function in homeostatic structural plasticity is mediated by its interaction with ephrinB2.

Stimulation with the ephrinB2 specific receptor EphB4 induces a dynamic AMPARs surface shift

We next attempted to force the stabilization of AMPARs at the membrane by stimulating the ephrinB2 pathway with its specific cognate receptor EphB4. Stimulation with the extracellular domain of the EphB4 receptor fused to Fc leads to the specific clustering and activation of ephrinB2 ligands and to membrane stabilization of AMPARs in hippocampal neurons (Essmann et al., 2008). Thus, we stimulated OTCs with EphB4-Fc or Fc as a control, and after expansion, we analyzed the distribution of GluA2-containing AMPARs in the different compartments. EphB4-Fc treatment resulted in a robust shift of AMPARs to the surface in all spine types (Figures 3C–3G). This increase

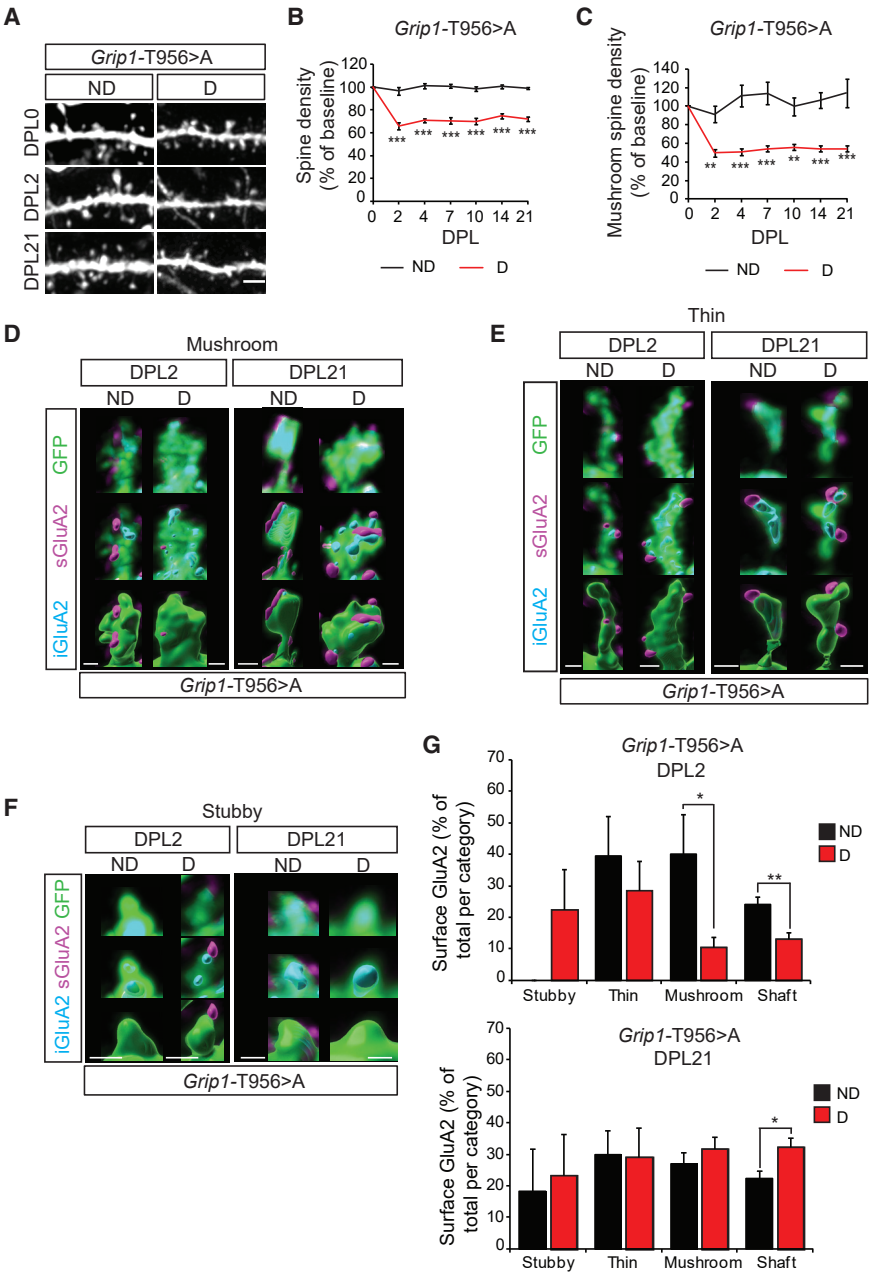

Figure 2. GRIP1 is required for AMPAR dynamics and mushroom spine recovery after lesion

(A) Representative pictures of dendritic stretches from non-denervated and denervated *Grip1* T956 > A OTCs.

(B and C) Quantification of spine (B) and mushroom spine density (C) as ratios to DPL0 corresponding to (A); n = 8–9 neurons per condition, 4 experiments.

(D–F) Representative reconstructions of mushroom (D), thin (E), and stubby (F) spines from non-denervated and denervated OTCs at DPL2 and DPL21.

(G) Quantification of surface GluA2 in D and ND OTCs, represented as percentage of total GluA2 per compartment; n = 5 neurons per condition, 2 experiments.

Scale bars: 2 μm (A), 1 μm (D)–(F). Graphs show means ± SEMs. *p < 0.05; **p < 0.01; ***p < 0.001. Exact p values in Table S1.

See also Figure S3.

was comparatively very prominent in stubby spines, where in control conditions almost all of the GluA2 is internal and rarely seen at the surface (compare to Figure 1E).

Surface AMPAR shift is sufficient to restore spine recovery after lesion

Since the endogenous GRIP1 protein is still present in *Grip1*-T956 > A mice, we hypothesized that stimulation with EphB4 would be able to stabilize sufficient surface GluA2-containing AMPARs that are bound to the endogenous GRIP1 and compensate the cytoskeletal trapping of GluA2-containing AMPARs bound to GRIP1 T956 > A. To address this, we denervated *Grip1*-T956 > A OTCs and stimulated them with EphB4-Fc as from DPL7, when recovery is first seen in denervated control OTCs (Figure 4A). Consistent with our previous findings that ephrinB2 reverse signaling promotes spine morphogenesis and maturation (Segura et al., 2007), EphB4-Fc treatment induced an increase in mushroom spine density in non-denervated control OTCs (Figures 4B and 4C). In denervated OTCs, while Fc-treated *Grip1*-T956 > A OTCs remained unable to recover after lesion, EphB4-Fc treatment of denervated *Grip1*-T956 > A OTCs significantly enhanced recovery of mushroom spine density, which nearly returned to baseline at DPL21 (Figures 4B and 4C). In addition, starting EphB4-Fc treatment at DPL0 significantly prevented mushroom spine loss after lesion both in *Grip1*-T956 > A and control OTCs. In both cases, spine densities dropped by <10% and nearly immediately returned to baseline levels (Figures 4D and 4E), indicating the crucial role that ephrinB2 plays in mushroom spine stability.

Finally, to correlate the rescue effect of EphB4-Fc treatment to dynamic AMPAR surface shifts, we analyzed GluA2-containing AMPAR distribution by expansion microscopy in *Grip1*-T956 > A OTCs at the end of the rescue experiment. The rescue observed in EphB4-Fc-stimulated denervated *Grip1*-T956 > A OTCs was highly correlated with a significant increase in surface GluA2 levels in mushroom spines that was not seen in the non-rescued control Fc-treated denervated *Grip1*-T956 > A OTCs (Figures 4F and 4G). Therefore, our results indicate a direct

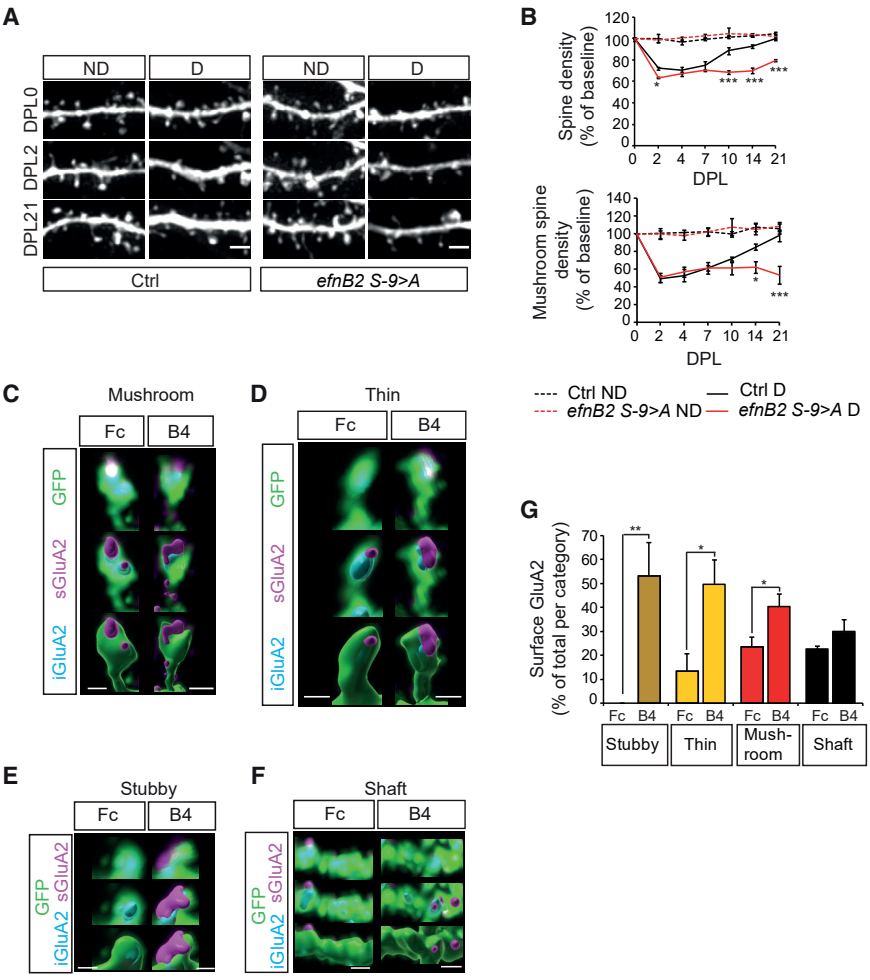

Figure 3. EphrinB2 mediates GRIP1 function in homeostatic plasticity and promotes surface AMPARs

(A) Representative pictures of dendritic stretches from ND and D *efnB2 S-9 > A* and Ctrl OTCs.

(B) Quantification of spine (upper graph) and mushroom spine density (lower graph) as ratios to DPL0 corresponding to (A). Significance levels shown for *efnB2 S-9 > A* D to Ctrl D; n = 5–7 neurons per condition, 3 experiments).

(C–F) Representative reconstructions of mushroom (C), thin (D), and stubby (E) spines, and shafts (F) from OTCs (at 21 days in culture) stimulated with EphB4-Fc (B4) or Fc control.

(G) Quantification of surface GluA2 in EphB4-Fc stimulated OTCs, represented as percentages of total GluA2 per compartment, corresponding to (C)–(E); n = 5 neurons per condition, 2 experiments.

Scale bars: 2 μm (A), 1 μm (C)–(F). Graphs show means ± SEMs. *p < 0.05; **p < 0.01; ***p < 0.001. Exact p values in Table S1.

See also Figure S4.

correlation between the stabilization of surface GluA2 and spine homeostatic structural plasticity after lesion.

DISCUSSION

AMPAR distribution is a crucial determinant for synaptic function and plasticity; the number of functional receptors at the synapse is directly related to its efficacy and is thus tightly regulated. Here, we addressed the distribution of GluA2-containing AMPARs in organotypic slice cultures—in other words, in stable, long-lasting 3-dimensional (3D) neuronal networks using expansion microscopy to obtain sufficient spatial resolution to differentiate surface and internal AMPARs. We used GFP signal as a proxy for the neuronal membrane to discriminate between these two pools and showed the validity of this method by combining permeabilized and non-permeabilized conditions in hippocampal cultures. Using this method, we have been able to visualize not only surface AMPARs but also cytoplasmic receptors, a significant difference from other methods such as live labeling or pre-embedding immunogold electron microscopy, while retaining a fine spatial discrimination power (Böger et al., 2019; Nair et al., 2013; Tao-Cheng et al., 2011). We have observed a primarily intracellular GluA2-containing AMPAR localization (88% on average). Intriguingly, this proportion is higher than has been previously observed by light or electron microscopy. However, the reported range is relatively wide, with intracellular receptors varying between 30% and 70% of all AMPARs, and our results are relatively close to the upper side of that spectrum (Hall and Soderling, 1997; Perestenko and Henley, 2003; Rubio and Wenthold, 1999). The strikingly similar distribution observed in CA1 pyramidal cells suggests that this pattern may reflect a more general behavior. Cultured hippocampal neurons also showed a largely intracellular AMPAR distribution (67% in mushroom spines), but this proportion was lower than our results in pyramidal and granule cells and falls within the upper range of the described spectrum. In addition to potential methodological reasons, this suggests that the difference between our results and the literature may be partially ascribed to the biological model (culture/slice). In all cases, however, our data consistently indicate a predominantly intracellular distribution of AMPARs, at least in hippocampal principal neurons. Further work on additional cell types will be required to determine how broadly this distribution is observed across neuronal types and could moreover address the subcellular distribution of the intracellular AMPARs (e.g., endosomes, spine apparatus, endoplasmic reticulum).

AMPARs react dynamically to plasticity-inducing stimuli, and a chronic reduction in network activity (e.g., following denervation) has been shown to induce an increase in synaptic AMPARs, likely as homeostatic compensation to maintain neuronal firing (Turrigiano, 2017). The effect on spine density and morphology, however, is more contrasted, as reductions, augmentations, or a lack of effect have been reported in response to various

CellPress
OPEN ACCESS

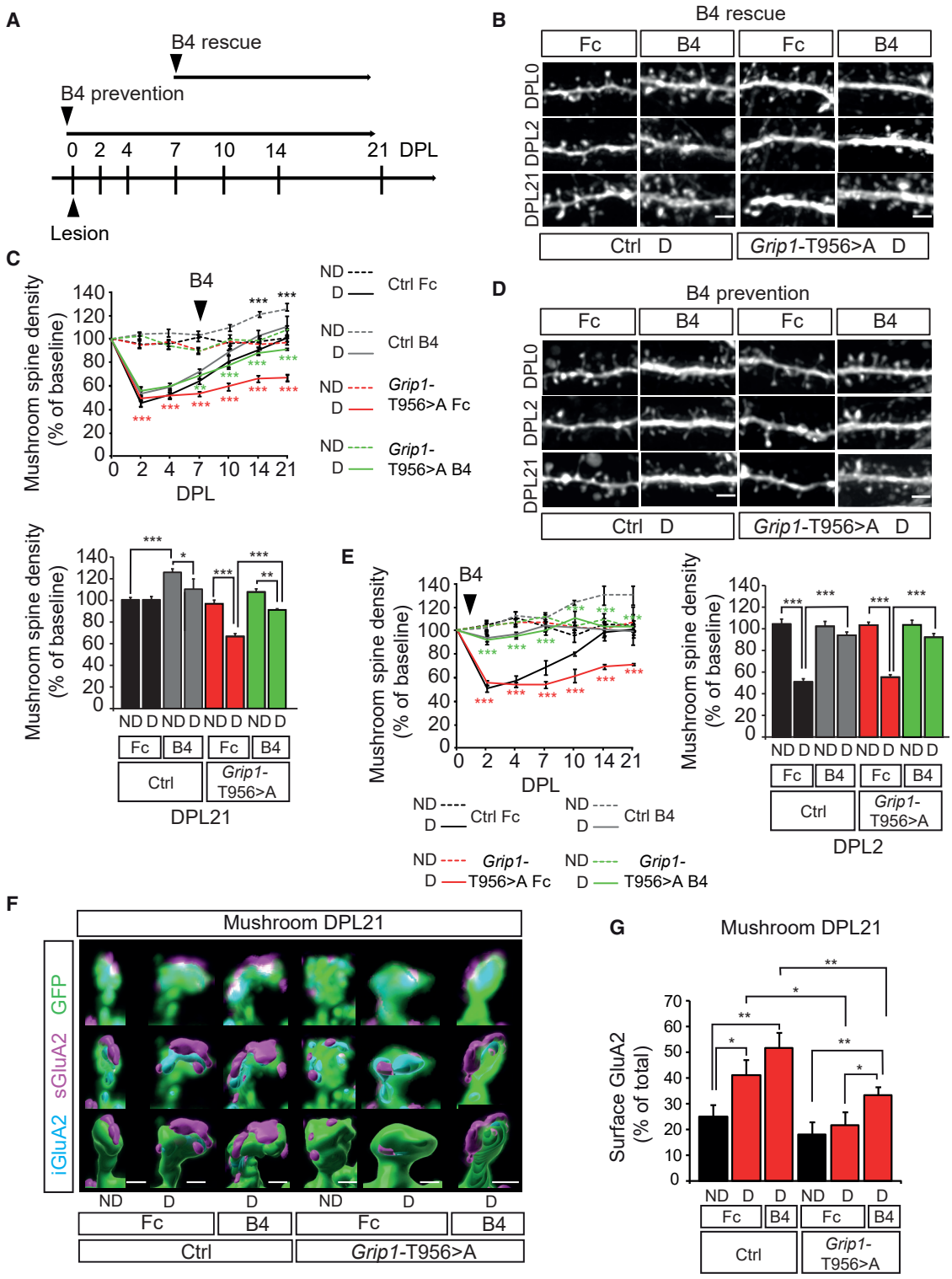

Figure 4. Stimulation with the ephrinB2 specific receptor EphB4 prevents denervation-induced spine loss and rescues GRIP1 deficiency

(A) Timeline of prevention and rescue experiments. EphB4-Fc treatment (B4).

(B) Representative pictures of dendritic stretches from dentate granule cells in denervated Ctrl and *Grip1* T956 > A OTCs following the rescue paradigm.

(legend continued on next page)

deprivation paradigms (Barnes et al., 2017; Hofer et al., 2009; Keck et al., 2013; Kirov et al., 2004; McKinney et al., 1999; Wallace and Bear, 2004). Consistent with the previous literature on the lesion model used in this study, we observe a marked spine loss upon lesion, with a gradual recovery to baseline (Perederiy and Westbrook, 2013; Vlachos et al., 2012a). We additionally report here that such loss is mainly borne by mushroom spines, and thus results in the specific loss of larger synapses. Moreover, the lesion induces a redistribution of GluA2-containing AMPARs toward the surface in the remaining thin and mushroom spines. These synchronous effects support a direct causative link between AMPAR activity and spine stability, whereby the increased surface AMPARs help stabilize the remaining spines, and later the newly formed spines, thus promoting the recovery of spine density. Consistently, the increase in surface GluA2-containing AMPARs persists until the last imaging session (DPL21), when spine density has already reached baseline. Our imaging results are in line with two studies in which pharmacological blockade of AMPARs in non-denervated OTCs decreased spine stability and led to spine loss, while incubating lesioned OTCs with AMPA could rescue spine loss (McKinney et al., 1999; Vlachos et al., 2013). A predominant postsynaptic mechanism supporting spine recovery is also consistent with previous reports showing that axonal sprouting in the outer layer of DG granule cells is highly restricted after lesion *in vivo*, and that most of the new spines are not faced with presynaptic partners (Perederiy et al., 2013; Del Turco et al., 2003).

We investigated the GluA2 subunit due to the predominance of GluA2-containing AMPARs in hippocampal neurons, the specific binding of GRIP1 to GluA2/A3, and the importance of GluA2 for homeostatic plasticity (Dong et al., 1997; Gainey et al., 2009; Wenthold et al., 1996). Changes in the distribution of GluA1-containing AMPARs have also been reported during homeostatic mechanisms (Soares et al., 2013; Thiagarajan et al., 2005), and it is thus possible that these AMPARs are also transported to the surface after denervation; if this is the case, then the lesion likely induces a concomitant shift in GluA1- and GluA2-containing AMPARs, as has been already reported during synaptic scaling (Wierenga et al., 2005).

Molecularly, we show that the physiological and morphological responses to lesion are altered in OTCs impaired for GRIP1 and ephrinB2 function, two proteins involved in a complex including GluA2 and mediating surface AMPAR insertion and stabilization (Essmann et al., 2008; Pfennig et al., 2017). GRIP1 has already been associated with promoting synaptic AMPAR stabilization and accumulation during homeostatic scaling up (Gainey et al., 2015; Tan et al., 2015). Based on our previous and current findings, we propose that these functions of GRIP1 are co-regulated by ephrinB2, which stabilizes GRIP1-bound GluA2-containing AMPARs at synaptic and extrasynaptic sites in the dendritic membrane. EphB4-Fc treatment, most likely through ephrinB2 activation, increases this stabilization, thus enhancing surface AMPARs at spines and shafts in non-denervated, wild-type conditions, while it can rescue the reduced surface GluA2-containing AMPAR levels to wild-type conditions in denervated mutant GRIP1 OTCs. This stabilization of receptors in turn promotes the stability of spines, specifically bigger spines, and thus their density, in agreement with spine stability being the primary parameter underlying density changes after lesion, a hypothesis that is further supported by the prevention of spine loss by immediate ephrinB2 activation. Mechanistically, a possible link between the ephrinB2/GRIP1/GluA2 complex and spine morphogenesis is the adhesion molecule N-cadherin, which is co-transported with GluA2 by GRIP1, binds the extracellular domain of GluA2, and supports spine morphogenesis by interacting with the actin cytoskeleton; blocking the co-transport reduces the number of spines and excitatory synapses (Heisler et al., 2014; Saglietti et al., 2007). In addition, we have previously shown that ephrinB ligands promote actin assembly and spine morphogenesis via the adaptor Grb4 and the actin regulator GIT1, which itself interacts with GRIP1 to mediate AMPAR trafficking (Ko et al., 2003; Segura et al., 2007). AMPAR activity has also been proposed to support spine formation and maturation, for instance, via the stabilization of the postsynaptic density or via the actin-interacting protein drebrin (De Roo et al., 2008; Takahashi et al., 2009). The addition of vesicles to the spine membrane during GRIP1-bound AMPAR insertion may also support the stabilization of surviving mushroom spines after lesion, similar to what has been described for recycling endosomes during constitutive conditions and after LTP (Park et al., 2006). Whether these pathways (or others) mediate the role of ephrinB2/GRIP1 during structural homeostatic plasticity remains open to investigation.

Collectively, our findings provide regulatory mechanistic insights as well as quantitative assessment of the correlation between changes in AMPAR dynamics and spine morphology during deprivation-induced homeostatic plasticity. Due to the involvement of the Eph/ephrin family in recovery after injury and neurological disorders (reviewed in Yang et al., 2018) and the association of GRIP1 with autism spectrum disorder (Han et al., 2017; Mejias et al., 2011), this cooperative mechanism

(C) Quantification of mushroom spine density as ratio to DPL0 (upper graph) corresponding to (B). Significance levels shown for Ctrl B4 ND relative to Ctrl Fc ND (black asterisks), for T956 > A Fc D to T956 > A Fc ND (red asterisks) and for T956 > A B4 D to T956 > A Fc D (green asterisks). Values corresponding to DPL21 are represented in the lower graph; n = 6–13 neurons per condition, 3 experiments.
(D) Representative pictures of dendritic stretches from dentate granule cells in denervated Ctrl and *Grip1* T956 > A OTCs following the prevention paradigm.
(E) Quantification of mushroom spine density as ratio to DPL0 (left graph). Significance levels shown for T956 > A Fc D to T956 > A Fc ND (red asterisks) and for T956 > A B4 D to T956 > A Fc D (green asterisks). Values corresponding to DPL2 are represented in the right graph; n = 4–10 neurons per condition, from 2–3 experiments.
(F) Representative reconstructions of mushroom spines from Fc- or EphB4-Fc (B4)-treated ND and D Ctrl or *Grip1* T956 > A OTCs at DPL21.
(G) Quantification of surface GluA2 represented as percentages of the total GluA2 found in a mushroom spine (n = 5 neurons per condition, 2 experiments).
Scale bars: 2 μm (B and D), 1 μm (F). Graphs show means ± SEMs. *$p < 0.05$; **$p < 0.01$; ***$p < 0.001$. Exact p values in Table S1.
See also Figure S4.

opens new avenues of research to promote dendritic spine recovery, not only upon injury but also in other pathological conditions.

STAR★METHODS

Detailed methods are provided in the online version of this paper and include the following:

- KEY RESOURCES TABLE
- RESOURCE AVAILABILITY
  - Lead contact
  - Materials availability
  - Data and code availability
- EXPERIMENTAL MODELS AND SUBJECT DETAILS
- METHOD DETAILS
  - Primary hippocampal cultures and new AMPA receptor insertion assay
  - Organotypic brain slice **dissection, culture and imaging**
  - OTC staining
  - Expansion microscopy
  - Dissection, fixation and staining of acute slices
  - Image acquisition and analysis
- QUANTIFICATION AND STATISTICAL ANALYSIS

SUPPLEMENTAL INFORMATION

Supplemental information can be found online at https://doi.org/10.1016/j.celrep.2021.108923.

ACKNOWLEDGMENTS

We thank E. Harde, A. Vlachos, and T. Deller for help with the lesion model; P. Donlin-Asp and A.-S. Hafner for help with the expansion microscopy; J. Bär and M. Mikhaylova for help with the Imaris software; U. Bauer, P. Brendel, D. Schmelzer, and T. Belefkih for technical support; and M. Segarra, J. Hefendehl, and H. Zimmermann for helpful discussions. This work was supported by grants from the Deutsche Forschungsgemeinschaft (SFB 834, SFB1080, SFB1193, FOR2325, EXC 115, EXC 147, EXC 2026), ERC_AdG_Neurovessel (project no. 669742), and the Max Planck Fellow Program and Gutenberg Research College (GRC) at Johannes Gutenberg University Mainz (to A.A.-P.).

AUTHOR CONTRIBUTIONS

D.B. designed, performed, and supervised the experiments and performed the analysis for the repetitive live imaging; M.K.K., performed the analysis of expansion microscopy experiments; F.F. supervised the experiments; J.H. performed the AMPA receptor new insertion assays; A.A.-P. designed and supervised all stages of the project; and D.B. and A.A.-P. wrote the manuscript. All of the authors discussed and interpreted the data and provided input on the written manuscript.

DECLARATION OF INTERESTS

The authors declare no competing interests.

Received: April 23, 2020
Revised: December 20, 2020
Accepted: March 9, 2021
Published: March 30, 2021

REFERENCES

Arendt, K.L., Sarti, F., and Chen, L. (2013). Chronic inactivation of a neural circuit enhances LTP by inducing silent synapse formation. J. Neurosci. *33*, 2087–2096.

Asano, S.M., Gao, R., Wassie, A.T., Tillberg, P.W., Chen, F., and Boyden, E.S. (2018). Expansion Microscopy: Protocols for Imaging Proteins and RNA in Cells and Tissues. Curr. Protoc. Cell Biol. *80*, e56.

Barberis, A. (2020). Postsynaptic plasticity of GABAergic synapses. Neuropharmacology *169*, 107643.

Barnes, S.J., Franzoni, E., Jacobsen, R.I., Erdelyi, F., Szabo, G., Clopath, C., Keller, G.B., and Keck, T. (2017). Deprivation-induced homeostatic spine scaling in vivo is localized to dendritic branches that have undergone recent spine loss. Neuron *96*, 871–882.e5.

Bissen, D., Foss, F., and Acker-Palmer, A. (2019). AMPA receptors and their minions: auxiliary proteins in AMPA receptor trafficking. Cell. Mol. Life Sci. *76*, 2133–2169.

Böger, C., Hafner, A.-S., Schlichthärle, T., Strauss, M.T., Malkusch, S., Endesfelder, U., Jungmann, R., Schuman, E.M., and Heilemann, M. (2019). Super-resolution imaging and estimation of protein copy numbers at single synapses with DNA-point accumulation for imaging in nanoscale topography. Neurophotonics *6*, 035008.

Chen, F.C., Tillberg, P.W., and Boyden, E.S. (2015). Expansion microscopy. Science *347*, 543–548.

De Roo, M., Klauser, P., Mendez, P., Poglia, L., and Muller, D. (2008). Activity-dependent PSD formation and stabilization of newly formed spines in hippocampal slice cultures. Cereb. Cortex *18*, 151–161.

Del Turco, D., Woods, A.G., Gebhardt, C., Phinney, A.L., Jucker, M., Frotscher, M., and Deller, T. (2003). Comparison of commissural sprouting in the mouse and rat fascia dentata after entorhinal cortex lesion. Hippocampus *13*, 685–699.

Dong, H., O'Brien, R.J., Fung, E.T., Lanahan, A.A., Worley, P.F., and Huganir, R.L. (1997). GRIP: a synaptic PDZ domain-containing protein that interacts with AMPA receptors. Nature *386*, 279–284.

Ehlers, M.D., Heine, M., Groc, L., Lee, M.C., and Choquet, D. (2007). Diffusional trapping of GluR1 AMPA receptors by input-specific synaptic activity. Neuron *54*, 447–460.

Essmann, C.L., Martinez, E., Geiger, J.C., Zimmer, M., Traut, M.H., Stein, V., Klein, R., and Acker-Palmer, A. (2008). Serine phosphorylation of ephrinB2 regulates trafficking of synaptic AMPA receptors. Nat. Neurosci. *11*, 1035–1043.

Feng, G., Mellor, R.H., Bernstein, M., Keller-Peck, C., Nguyen, Q.T., Wallace, M., Nerbonne, J.M., Lichtman, J.W., and Sanes, J.R. (2000). Imaging neuronal subsets in transgenic mice expressing multiple spectral variants of GFP. Neuron *28*, 41–51.

Forrest, M.P., Parnell, E., and Penzes, P. (2018). Dendritic structural plasticity and neuropsychiatric disease. Nat. Rev. Neurosci. *19*, 215–234.

Gähwiler, B.H. (1981). Morphological differentiation of nerve cells in thin organotypic cultures derived from rat hippocampus and cerebellum. Proc. R. Soc. Lond. B Biol. Sci. *211*, 287–290.

Gainey, M.A., Hurvitz-Wolff, J.R., Lambo, M.E., and Turrigiano, G.G. (2009). Synaptic scaling requires the GluR2 subunit of the AMPA receptor. J. Neurosci. *29*, 6479–6489.

Gainey, M.A., Tatavarty, V., Nahmani, M., Lin, H., and Turrigiano, G.G. (2015). Activity-dependent synaptic GRIP1 accumulation drives synaptic scaling up in response to action potential blockade. Proc. Natl. Acad. Sci. USA *112*, E3590–E3599.

Geiger, J.C., Lipka, J., Segura, I., Hoyer, S., Schlager, M.A., Wulf, P.S., Weinges, S., Demmers, J., Hoogenraad, C.C., and Acker-Palmer, A. (2014). The GRIP1/14-3-3 pathway coordinates cargo trafficking and dendrite development. Dev. Cell *28*, 381–393.

Grunwald, I.C., Korte, M., Adelmann, G., Plueck, A., Kullander, K., Adams, R.H., Frotscher, M., Bonhoeffer, T., and Klein, R. (2004). Hippocampal plasticity requires postsynaptic ephrinBs. Nat. Neurosci. *7*, 33–40.

Hall, R.A., and Soderling, T.R. (1997). Quantitation of AMPA receptor surface expression in cultured hippocampal neurons. Neuroscience *78*, 361–371.

Han, M., Mejias, R., Chiu, S.L., Rose, R., Adamczyk, A., Huganir, R., and Wang, T. (2017). Mice lacking GRIP1/2 show increased social interactions and enhanced phosphorylation at GluA2-S880. Behav. Brain Res. *321*, 176–184.

Heisler, F.F., Lee, H.K., Gromova, K.V., Pechmann, Y., Schurek, B., Ruschkies, L., Schroeder, M., Schweizer, M., and Kneussel, M. (2014). GRIP1 interlinks N-cadherin and AMPA receptors at vesicles to promote combined cargo transport into dendrites. Proc. Natl. Acad. Sci. USA *111*, 5030–5035.

Henley, J.M., and Wilkinson, K.A. (2016). Synaptic AMPA receptor composition in development, plasticity and disease. Nat. Rev. Neurosci. *17*, 337–350.

Hofer, S.B., Mrsic-Flogel, T.D., Bonhoeffer, T., and Hübener, M. (2009). Experience leaves a lasting structural trace in cortical circuits. Nature *457*, 313–317.

Hoogenraad, C.C., Milstein, A.D., Ethell, I.M., Henkemeyer, M., and Sheng, M. (2005). GRIP1 controls dendrite morphogenesis by regulating EphB receptor trafficking. Nat. Neurosci. *8*, 906–915.

Humpel, C. (2015). Organotypic brain slice cultures: a review. Neuroscience *305*, 86–98.

Jiang, N., Kim, H.J., Chozinski, T.J., Azpurua, J.E., Eaton, B.A., Vaughan, J.C., and Parrish, J.Z. (2018). Superresolution imaging of Drosophila tissues using expansion microscopy. Mol. Biol. Cell *29*, 1413–1421.

Keck, T., Keller, G.B., Jacobsen, R.I., Eysel, U.T., Bonhoeffer, T., and Hübener, M. (2013). Synaptic scaling and homeostatic plasticity in the mouse visual cortex in vivo. Neuron *80*, 327–334.

Kharazia, V.N., and Weinberg, R.J. (1997). Tangential synaptic distribution of NMDA and AMPA receptors in rat neocortex. Neurosci. Lett. *238*, 41–44.

Kirkwood, A., Rioult, M.G., and Bear, M.F. (1996). Experience-Dependent Modification of Synaptic Plasticity in Visual Cortex. Nature *381*, 526–528.

Kirov, S.A., Goddard, C.A., and Harris, K.M. (2004). Age-dependence in the homeostatic upregulation of hippocampal dendritic spine number during blocked synaptic transmission. Neuropharmacology *47*, 640–648.

Ko, J., Kim, S., Valtschanoff, J.G., Shin, H., Lee, J.-R., Sheng, M., Premont, R.T., Weinberg, R.J., and Kim, E. (2003). Interaction between liprin-alpha and GIT1 is required for AMPA receptor targeting. J. Neurosci. *23*, 1667–1677.

Ku, T., Swaney, J., Park, J.Y., Albanese, A., Murray, E., Cho, J.H., Park, Y.G., Mangena, V., Chen, J., and Chung, K. (2016). Multiplexed and scalable super-resolution imaging of three-dimensional protein localization in size-adjustable tissues. Nat. Biotechnol. *34*, 973–981.

Li, J., Park, E., Zhong, L.R., and Chen, L. (2019). Homeostatic synaptic plasticity as a metaplasticity mechanism - a molecular and cellular perspective. Curr. Opin. Neurobiol. *54*, 44–53.

Matsuzaki, M., Ellis-Davies, G.C.R., Nemoto, T., Miyashita, Y., Iino, M., and Kasai, H. (2001). Dendritic spine geometry is critical for AMPA receptor expression in hippocampal CA1 pyramidal neurons. Nat. Neurosci. *4*, 1086–1092.

Matsuzaki, M., Honkura, N., Ellis-Davies, G.C.R., and Kasai, H. (2004). Structural basis of long-term potentiation in single dendritic spines. Nature *429*, 761–766.

McKinney, R.A., Capogna, M., Dürr, R., Gähwiler, B.H., and Thompson, S.M. (1999). Miniature synaptic events maintain dendritic spines via AMPA receptor activation. Nat. Neurosci. *2*, 44–49.

Mejias, R., Adamczyk, A., Anggono, V., Niranjan, T., Thomas, G.M., Sharma, K., Skinner, C., Schwartz, C.E., Stevenson, R.E., Fallin, M.D., et al. (2011). Gain-of-function glutamate receptor interacting protein 1 variants alter GluA2 recycling and surface distribution in patients with autism. Proc. Natl. Acad. Sci. USA *108*, 4920–4925.

Nair, D., Hosy, E., Petersen, J.D., Constals, A., Giannone, G., Choquet, D., and Sibarita, J.-B. (2013). Super-resolution imaging reveals that AMPA receptors inside synapses are dynamically organized in nanodomains regulated by PSD95. J. Neurosci. *33*, 13204–13224.

Noguchi, J., Nagaoka, A., Watanabe, S., Ellis-Davies, G.C.R., Kitamura, K., Kano, M., Matsuzaki, M., and Kasai, H. (2011). In vivo two-photon uncaging of glutamate revealing the structure-function relationships of dendritic spines in the neocortex of adult mice. J. Physiol. *589*, 2447–2457.

Park, M., Salgado, J.M., Ostroff, L., Helton, T.D., Robinson, C.G., Harris, K.M., and Ehlers, M.D. (2006). Plasticity-induced growth of dendritic spines by exocytic trafficking from recycling endosomes. Neuron *52*, 817–830.

Peredériy, J.V., and Westbrook, G.L. (2013). Structural plasticity in the dentate gyrus—revisiting a classic injury model. Front. Neural Circuits *7*, 17.

Peredériy, J.V., Luikart, B.W., Washburn, E.K., Schnell, E., and Westbrook, G.L. (2013). Neural injury alters proliferation and integration of adult-generated neurons in the dentate gyrus. J. Neurosci. *33*, 4754–4767.

Perestenko, P.V., and Henley, J.M. (2003). Characterization of the intracellular transport of GluR1 and GluR2 α-amino-3-hydroxy-5-methyl-4-isoxazole propionic acid receptor subunits in hippocampal neurons. J. Biol. Chem. *278*, 43525–43532.

Pernal, S.P., Liyanaarachchi, A., Gatti, D.L., Formosa, B., Pulvender, R., Kuhn, E.R., Ramos, R., Naik, A.R., George, K., Arslanturk, S., et al. (2020). Nanoscale imaging using differential expansion microscopy. Histochem. Cell Biol. *153*, 469–480.

Pfennig, S., Foss, F., Bissen, D., Harde, E., Treeck, J.C., Segarra, M., and Acker-Palmer, A. (2017). GRIP1 Binds to ApoER2 and EphrinB2 to Induce Activity-Dependent AMPA Receptor Insertion at the Synapse. Cell Rep. *21*, 84–96.

Rochefort, N.L., and Konnerth, A. (2012). Dendritic spines: from structure to in vivo function. EMBO Rep. *13*, 699–708.

Rubio, M.E., and Wenthold, R.J. (1999). Differential distribution of intracellular glutamate receptors in dendrites. J. Neurosci. *19*, 5549–5562.

Saglietti, L., Dequidt, C., Kamieniarz, K., Rousset, M.C., Valnegri, P., Thoumine, O., Beretta, F., Fagni, L., Choquet, D., Sala, C., et al. (2007). Extracellular interactions between GluR2 and N-cadherin in spine regulation. Neuron *54*, 461–477.

Scheefhals, N., and MacGillavry, H.D. (2018). Functional organization of postsynaptic glutamate receptors. Mol. Cell. Neurosci. *91*, 82–94.

Schneider, C.A., Rasband, W.S., and Eliceiri, K.W. (2012). NIH Image to ImageJ: 25 years of image analysis. Nat. Methods *9*, 671–675.

Segura, I., Essmann, C.L., Weinges, S., and Acker-Palmer, A. (2007). Grb4 and GIT1 transduce ephrinB reverse signals modulating spine morphogenesis and synapse formation. Nat. Neurosci. *10*, 301–310.

Setou, M., Seog, D.H., Tanaka, Y., Kanai, Y., Takei, Y., Kawagishi, M., and Hirokawa, N. (2002). Glutamate-receptor-interacting protein GRIP1 directly steers kinesin to dendrites. Nature *417*, 83–87.

Soares, C., Lee, K.F.H., Nassrallah, W., and Béïque, J.-C. (2013). Differential subcellular targeting of glutamate receptor subtypes during homeostatic synaptic plasticity. J. Neurosci. *33*, 13547–13559.

Takahashi, H., Yamazaki, H., Hanamura, K., Sekino, Y., and Shirao, T. (2009). Activity of the AMPA receptor regulates drebrin stabilization in dendritic spine morphogenesis. J. Cell Sci. *122*, 1211–1219.

Tan, H.L., Queenan, B.N., and Huganir, R.L. (2015). GRIP1 is required for homeostatic regulation of AMPAR trafficking. Proc. Natl. Acad. Sci. USA *112*, 10026–10031.

Tao-Cheng, J.-H., Crocker, V.T., Winters, C.A., Azzam, R., Chludzinski, J., and Reese, T.S. (2011). Trafficking of AMPA receptors at plasma membranes of hippocampal neurons. J. Neurosci. *31*, 4834–4843.

Thiagarajan, T.C., Lindskog, M., and Tsien, R.W. (2005). Adaptation to synaptic inactivity in hippocampal neurons. Neuron *47*, 725–737.

Torres, R., Firestein, B.L., Dong, H., Staudinger, J., Olson, E.N., Huganir, R.L., Bredt, D.S., Gale, N.W., and Yancopoulos, G.D. (1998). PDZ proteins bind, cluster, and synaptically colocalize with Eph receptors and their ephrin ligands. Neuron *21*, 1453–1463.

Tronche, F., Kellendonk, C., Kretz, O., Gass, P., Anlag, K., Orban, P.C., Bock, R., Klein, R., and Schütz, G. (1999). Disruption of the glucocorticoid receptor gene in the nervous system results in reduced anxiety. Nat. Genet. *23*, 99–103.

Turrigiano, G.G. (2017). The dialectic of Hebb and homeostasis. Philos. Trans. R. Soc. Lond. B Biol. Sci. *372*, 20160258.

Turrigiano, G.G., Leslie, K.R., Desai, N.S., Rutherford, L.C., and Nelson, S.B. (1998). Activity-dependent scaling of quantal amplitude in neocortical neurons. Nature *391*, 892–896.

Vlachos, A., Bas Orth, C., Schneider, G., and Deller, T. (2012a). Time-lapse imaging of granule cells in mouse entorhino-hippocampal slice cultures reveals changes in spine stability after entorhinal denervation. J. Comp. Neurol. *520*, 1891–1902.

Vlachos, A., Becker, D., Jedlicka, P., Winkels, R., Roeper, J., and Deller, T. (2012b). Entorhinal denervation induces homeostatic synaptic scaling of excitatory postsynapses of dentate granule cells in mouse organotypic slice cultures. PLoS ONE *7*, e32883.

Vlachos, A., Helias, M., Becker, D., Diesmann, M., and Deller, T. (2013). NMDA-receptor inhibition increases spine stability of denervated mouse dentate granule cells and accelerates spine density recovery following entorhinal denervation in vitro. Neurobiol. Dis. *59*, 267–276.

Wallace, W., and Bear, M.F. (2004). A morphological correlate of synaptic scaling in visual cortex. J. Neurosci. *24*, 6928–6938.

Wenthold, R.J., Petralia, R.S., Blahos J, I.I., and Niedzielski, A.S. (1996). Evidence for multiple AMPA receptor complexes in hippocampal CA1/CA2 neurons. J. Neurosci. *16*, 1982–1989.

Wierenga, C.J., Ibata, K., and Turrigiano, G.G. (2005). Postsynaptic expression of homeostatic plasticity at neocortical synapses. J. Neurosci. *25*, 2895–2905.

Yang, J.S., Wei, H.X., Chen, P.P., and Wu, G. (2018). Roles of Eph/ephrin bidirectional signaling in central nervous system injury and recovery. Exp. Ther. Med. *15*, 2219–2227.

Zhao, Y., Bucur, O., Irshad, H., Chen, F., Weins, A., Stancu, A.L., Oh, E.Y., DiStasio, M., Torous, V., Glass, B., et al. (2017). Nanoscale imaging of clinical specimens using pathology-optimized expansion microscopy. Nat. Biotechnol. *35*, 757–764.

Zhou, Q., Homma, K.J., and Poo, M.M. (2004). Shrinkage of dendritic spines associated with long-term depression of hippocampal synapses. Neuron *44*, 749–757.

STAR★METHODS

KEY RESOURCES TABLE

REAGENT or RESOURCE	SOURCE	IDENTIFIER
Antibodies		
Mouse monoclonal anti-GluA2 (extracellular epitope, clone 6C4)	Millipore	Cat # MAB397; RRID: AB_2113875
Chicken polyclonal anti-GFP	Abcam	Cat # ab13970; RRID: AB_300798
Rabbit polyclonal anti-MAP2	Chemicon	Cat # AB5622; RRID: AB_91939
Donkey polyclonal anti-chicken Alexa 488	Dianova	Cat# 703-546-155; RRID: AB_2340376
Donkey polyclonal anti-mouse Alexa 568	Molecular Probes	Cat # A10037; RRID: AB_2534013
Goat anti-mouse STAR 635P	Abberior	Cat # 2-0002-007-5
Donkey polyclonal anti-mouse Cy3	Dianova	Cat # 715-165-151; RRID: AB_2315777
Donkey polyclonal anti-rabbit Alexa 488	Molecular Probes	Cat # A21206; RRID: AB_2535792
Unconjugated polyclonal anti-mouse IgG	Dianova	Cat # 715-005-150; RRID: AB_2340758
Chemicals, peptides, and recombinant proteins		
Recombinant mouse EphB4-Fc chimera protein	R&D Systems	Cat # 446-B4-200
ChromPure human IgG, Fc fragment	Dianova	Cat # 009-000-008; RRID: AB_2337046
Donkey anti-human IgG, Fc fragment	Dianova	Cat # 709-005-098; RRID: AB_2340482
Critical commercial assays		
Lipofectamine LTX and Plus Reagent	Invitrogen	15338-100
Experimental models: Organisms/strains		
Mouse: Tg(Nes-cre)^{1Kln}	Tronche et al., 1999	MGI ID: 2176173
Mouse: Tg(Thy1-EGFP)^{MJrs}	Feng et al., 2000	MGI ID: 3766828
Mouse: Efnb2^{tm4Kln}	Grunwald et al., 2004	MGI ID: 3026687
Mouse: *efnB2 S-9 > A*	Pfennig et al., 2017	In house
Mouse: *Grip1*-T956 > A	Geiger et al., 2014	In house
Mouse: C57BL/6J	Jackson Laboratories	JAX: #000664
Recombinant DNA		
Plasmid: pAcGFP1-N1	Clontech	Snapgene
Software and algorithms		
Huygens Professional 17.04-19.10	Scientific Volume Imaging	https://svi.nl/HomePage
ImageJ 5.12	Schneider et al., 2012	https://imagej.nih.gov/ij/
Imaris 9.0-9.6	Bitplane	https://imaris.oxinst.com/
MetaMorph 7.7	Molecular Devices	https://www.moleculardevices.com/products/cellular-imaging-systems/acquisition-and-analysis-software/metamorph-microscopy
GraphPad 6	Prism	https://www.graphpad.com/

RESOURCE AVAILABILITY

Lead contact

Further information and requests for resources and reagents should be directed to and will be fulfilled by the Lead Contact, Amparo Acker-Palmer (acker-palmer@bio.uni-frankfurt.de).

Materials availability

This study did not generate new reagents.

Data and code availability

The dataset supporting this study are available from the corresponding author upon request.

EXPERIMENTAL MODELS AND SUBJECT DETAILS

Mice were kept in a 12h dark/light cycle with food and water *ad libitum*. Males and females were kept separately unless for breeding purposes. The generation of the *Grip1*-T956 > A mouse line has been previously described (Geiger et al., 2014), as well as of the conditional *efnB2*$^{lox/lox}$ mouse line (Efnb2^{tm4Kln}; Grunwald et al., 2004), the knock-in *efnB2 S-9 > A* (Pfennig et al., 2017), and the (Nes)cre line (Tg(Nes-cre)^{1Kln}; Tronche et al., 1999). For all experiments but the newly inserted assay, these lines were crossed to the Tg(Thy1-EGFP) reporter line (Tg(Thy1-EGFP)^{MJrs}; Feng et al., 2000). For the key findings, experimental animals were pups sacrificed at postnatal day 3 to 5 for organotypic slice cultures. Pups of either sex were used; due to their very young age and the maturation time of the organotypic slice cultures (3 weeks) in a body-less environment, minimal to no effects of sex should be expected. For restricted supporting experiments (Figures S1A–S1E, S3A, and S3B), embryos at embryonic day 16.5-18.5 were used for primary hippocampal cultures. During dissection, neurons from all embryos of the same genotype (regardless of sex) were pooled. For a single supporting experimental dataset (Figures S1J–S1L), adult female mice at postnatal day 40 were used to prepare acute slices. For all animals, genotypes were determined by PCR using corresponding primers on mouse tail DNA. Tails were digested for 50min in 100 μL 50mM NaOH at 95°C, then the digestion was stopped by addition of 10 μL 1.5M Tris-HCl pH 8.8. PCR reactions were performed in 25 μL volume containing 1-2 μL DNA, 20.55-19.55 μL distilled water, 2.5 μL ThermoPol reaction buffer (New England Biolabs), 0.2 μL deoxynucleotide (dNTP) solution mix (New England Biolabs), 0.25 μL of each primer, 1 μL Taq polymerase (New England BioLabs) (*Grip1*, (Nes)cre, (Thy1)EGFP); or 2 μL DNA, 9.75 μL distilled water, 12.5 μL Go Green Taq master mix (Promega), 0.25 μL of each primer (*efnB2*$^{lox/lox}$, *efnB2 S-9 > A*).

All animal use was performed in compliance with the governmental authorities of Hessen and followed the German animal welfare legislation.

METHOD DETAILS

Primary hippocampal cultures and new AMPA receptor insertion assay

Primary hippocampal cultures were dissected from mouse embryos at embryonic day 16.5-E18.5. Pregnant dams were sacrificed by cervical dislocation and embryos were removed and kept on ice; the hippocampi were dissected in pre-chilled dissection medium (Hank's balanced salt solution (HBSS) with 1% Pen/Strep, 1% GlutaMax, 1% HEPES), digested in 1ml trypsin-EDTA for 15min at 37°C, washed twice in pre-warmed serum medium (Dulbecco's modified Eagle medium (DMEM) with 10% fetal bovine serum (FBS)) and twice in pre-warmed NB+ medium (Neurobasal medium supplemented with 2mM Glutamax, 77.7mM D-Glucose). Neurons were then gently dissociated with a fire-polished Pasteur pipette, centrifugated for 5min at 71 g, and finally plated at 40,000 cells/cm^2. Neurons were kept in NB++ medium (Neurobasal medium supplemented with 2mM Glutamax, 77.7mM D-Glucose and 1:50 B27) at 37°C and 5% CO2 for 13 to 14 days until fixation. For subsequent staining and expansion microscopy, neurons were transfected with a plasmid expressing GFP at 10 days *in vitro* (DIV) using the Lipofectamine LTX kit (Invitrogen) according to the manufacturer's instructions. At 14 DIV, neurons were fixed (4% PFA/PBS with 4% sucrose) for 10 min on ice, washed with NH_4Cl for 10 min on ice, blocked in blocking buffer (2% BSA/4% NDS/PBS) for 30 min at room temperature, incubated overnight with mouse anti-GluA2 antibody (1:500 in blocking buffer) at 4°C and labeled with donkey-anti-mouse Alexa 568 (1:200 in blocking buffer) for 1h at room temperature. For the visualization of extra- and intracellular GluA2, neurons were subsequently permeabilized for 5 min in 0.1% Triton X-100 in PBS, blocked for 30 min, incubated overnight with the same mouse anti-GluA2 (1:500) and with chicken anti-GFP (1:1000), and labeled with goat anti-mouse Abberior STAR 635P (1:200) and donkey anti-chicken Alexa 488 (1:500).

All neurons from mutant and control littermates were always dissected, stained, imaged and analyzed in the same experimental conditions on the same day. After 14 DIV, neurons were used for the new AMPAR insertion assay as described before (Pfennig et al., 2017). Briefly, neurons were incubated on ice for 30 min with anti-GluA2 antibody in blocking medium (NB++ with 2% bovine serum albumin (BSA) and 4% normal donkey serum (NDS)), followed by an incubation on ice for 30 min with unconjugated anti-mouse IgG (1:200) in NB++ medium. Neurons were then returned to the incubator in their original medium for 3h and stimulated (if applicable) for 10 min with 10mM KCl at the start of the 3h incubation. Afterward, they were fixed and processed for immunocytochemistry in non-permeabilizing conditions as described above: neurons were blocked in blocking buffer for 30 min at room temperature, stained overnight at 4°C with the same anti-GluA2 antibody (1:500), as well as rabbit anti-MAP2 (1:1000) as control for cell membrane integrity, in blocking buffer, and labeled with the corresponding secondary antibodies (anti-mouse-Cy3 and anti-rabbit Alexa 488, 1:500) in blocking buffer for 1h at room temperature before mounting with Prolong Antifade Kit.

Organotypic brain slice dissection, culture and imaging

Organotypic brain slice cultures (OTCs) were prepared from pups at P3-P5 from *Grip1*-T956 > A, *Nes cre;efnB2*$^{lox/lox}$, *efnB2 S-9 > A* transgenic mice and control mice all crossed to Tg(Thy1-EGFP) reporter mice. All OTCs from mutant and control littermates were always dissected and subsequently processed in the same experimental session on the same day. Horizontal slices were sectioned

using a vibratome (Leica, VT1200S) in cold preparation medium (modified Eagle's medium (MEM), 25mM 4-(2-hydroxyethyl)-1-piperazineethanesulfonic acid (HEPES) buffer solution, 2mM Glutamax, 0.45% D-Glucose, 0.1 mg/ml streptomycin, 100 U/ml penicillin) at pH 7.4. Around 4-6 slices containing the hippocampal formation were collected per mouse, from which the two hippocampal formations per slice were carefully dissected under a binocular microscope. Only slices where the dentate gyrus showed its typical "V" shape were kept. All OTCs from one mouse (i.e., 8-12 hippocampal formations) were equally divided between two wells in a six-well plate and transferred on a cell culture insert (Millipore). OTCs were then cultivated in an incubator at 35°C for 18-21 days for stabilization and maturation. The incubation medium (42% MEM, 25% basal medium eagle (BME), 25% normal horse serum, 25mM HEPES, 0.65% D-glucose, 0.15% $NaHCO_3$, 0.1mg/ml streptomycin, 100U/ml penicillin, 2mM Glutamax; + 1mg/ml Amphotericin B for prevention and rescue experiments) was replaced three days per week and the pH adjusted to 7.3 every time.

Imaging experiments started 18-21 days after dissection. Per insert, one OTC was selected as a non-denervated control and one for entorhinal cortex lesion (ECL), which was performed immediately after the first imaging session by cutting and removing the entorhinal cortex using a sterile scalpel under a binocular microscope. Per OTC, 1-2 granule cells were selected in the supra- or infrapyramidal blade; no difference was found in lesion-induced changes (data not shown) and all cells were pooled regardless of location. One secondary dendritic stretch in the outer molecular layer, defined as > 50μm from the soma, was imaged per neuron. For prevention and rescue experiments, one insert per mouse was stimulated with EphB4-Fc, while the other was treated with Fc as a control. 3μg EphB4-Fc and 3μg Fc were pre-clustered with 0.3μg donkey-anti-Fc for 1h at room temperature and were added to the corresponding wells every day, immediately after the first imaging session (day post lesion (DPL) 0, prevention) or one week later (DPL7) until the penultimate experimental day. For imaging, the insert was transferred to a single 35mm Petri dish (Greiner) and covered in imaging medium (120mM NaCl, 10mM HEPES, 4.2mM D-glucose, 4mM KCl, 2mM $CaCl_2$, 1mM $MgCl_2$, 0.1mM Trolox, 0.1mg/ml streptomycin, 100U/ml penicillin; pH 7.4 and osmolarity matching the incubation medium; + 1mg/ml Amphotericin B for prevention and rescue experiments) pre-warmed to 35°C.

OTC staining

OTCs at two or twenty-one days post lesion (DPL2 or DPL21) were fixed in ice-cold 4% PFA/PBS for 5min, washed extensively in PBS to remove excess PFA, and processed for immunohistochemistry as floating sections after being gently scraped from the inserts. A high level of permeabilization was found necessary to allow correct antibody penetration, and all steps were performed in the same blocking buffer (2% Triton X-100/3% normal donkey serum (NDS)/3% normal goat serum (NGS) in PBS). After 2h blocking, OTCs were incubated with chicken anti-GFP (1:1000) and mouse anti-GluA2 (1:500) for one week at 4°C and subsequently with the corresponding secondary antibodies (anti-chicken Alexa 488 and anti-mouse Alexa 568, 1:500) for 3 days at 4°C.

Expansion microscopy

Expansion microscopy in hippocampal cultures was performed exactly according to the protocol for neuronal cultures described in Asano et al. (2018) (basic protocol 1). Briefly, the coverslips were transferred singularly into the 10mm microwell of 35mm dishes (MatTek). Neurons were incubated with 0.1mg/ml Acryloyl-X-SE/DMSO for 3h at room temperature. Freshly prepared gelling solution (47:1:1:1 Stock X (in g/100ml solution: 8.6 sodium acrylate, 2.5 acrylamide, 0.15 N,N-methylenebisacrylamide, 11.7 NaCl, 1x PBS, in water): tetramethylethylenediamine (TEMED): ammonium persulfate (APS): distilled water) was added to each microwell and covered by a 15mm coverslip to ensure the formation of a smooth, flat and thin gel. The coverslips were then incubated for 1h at 37°C for complete polymerization. Afterward, the coverslip was carefully removed and the gels were completely covered in 2ml digestion buffer/dish (in 100ml solution: 0.5g Triton X-100, 0.2ml EDTA disodium (pH 0.8), 5ml Triton-Cl (1M, pH 8.0), 4.67 g NaCl, in water) with Proteinase K (800U/ml) and incubated overnight at room temperature. Gels were then expanded in distilled water (6 successive baths, 20 min each). Gels were mounted immediately prior imaging to prevent dehydration in 2% low-melt agarose to minimize movement; no agarose was poured on top of the gel to prevent diffraction.

Expansion microscopy for OTCs was performed according to the protocol for intact tissues described in Asano et al. (2018) (basic protocol 2). The process is exactly as described above, with the following differences: the incubation in Acryloyl-X-SE/DMSO lasted overnight instead of 3h; the gelling solution contained 4-hydroxy-TEMPO (4HT) instead of distilled water (in the same ratio); and the OTCs were first incubated with 200μl gelling solution/microwell for 30 min at 4°C to allow deep penetration of the gelling solution in the tissue, before being incubated with fresh 150μl solution/microwell for 2h at 37°C to ensure complete gelation.

Dissection, fixation and staining of acute slices

Acute, coronal slices were prepared from adult female mice (postnatal day 40) at a thickness of 400 μm (Campden Microtome 7000smz) in ice-cold ACSF (125 mM NaCl, 3 mM KCl, 1.25 mM NaH_2PO_4, 26 mM $NaHCO_3$, 2 mM $CaCl_2$, 1mM $MgSO_4$ and 10 mM glucose, bubbled with 95% O_2 and 5% CO_2, pH 7.4). Slices recovered in a submerged chamber in ACSF at 35°C for 30 min, were transferred to a six-well plate and laid on a cell culture insert (Millipore) and recovered for 30 min at 35°C. Slices were fixed 4% PFA/PBS for 20mn, permeabilized with 0.4% Triton X-100 in PBS for 30mn, blocked for 1h in blocking buffer (0.2% Triton X-100/2% NDS in PBS), stained with chicken anti-GFP (1:500) in blocking buffer overnight at 4°C, and labeled with donkey-anti-chicken Alexa 488 in 0.5% goat serum/PBS for 2h. Slices were then processed for expansion microscopy exactly as described for organotypic slice cultures.

Image acquisition and analysis

For the new AMPAR insertion assay, neuronal cultures were imaged with a 63x objective (Zeiss) using a digital camera (Spot Pursuit, Diagnostic Instruments) attached to an epifluorescence microscope (Zeiss Axio Imager.M1). A fixed threshold was applied to all pictures of a given experiment to exclude background fluorescence and GluA2 staining intensity was quantified in manually determined dendritic stretches as the integrated fluorescence intensity divided by the area using MetaMorph (Molecular Devices). Experimental sets in which depolarization with KCl does not lead to an increased *de novo* AMPAR insertion in wild-type neurons are not included in the analysis.

For randomization of repetitive live imaging or expansion experiments, care was taken to allocate pups from the same litter and genotype to different treatment groups as evenly as possible. For spine analysis in OTCs, OTCs were imaged using a two-photon microscope (Leica, TCS SP8 MP) with a laser wavelength of 900nm. For orientation, a picture was taken of the OTC using the 10x objective at the first imaging session and the selected granule cells marked; additionally, a picture of the whole granule cells was also taken at 63x to identify the chosen dendritic stretch in the future imaging sessions. Granule cells located in the dorsal and ventral blade were used for this study; as no difference in spine density after lesion was found (data not shown), the data from all cells were pooled for quantification. One dendritic segment was imaged per granule cell and 1-4 granule cells per OTC. For analysis, z stacks of secondary dendritic stretches in the outer molecular layer (> 50μm from the soma) were captured using a water-dipping 63x objective (0.9 NA, 3x zoom). After deconvolution using the Classic Maximum Likelihood Estimation (CMLE) algorithm (automated parameters) of Huygens Professional (Scientific Volume Imaging), spines were automatically reconstructed and manually adjusted using the Filament Tracer module of Imaris (Bitplane). Spines were subsequently classified using the ''Classify Spines'' Imaris extension with the following morphological criteria: mushroom spines were identified first as spines with spine head maximal width $\geq$ 1.1 neck mean width and spine head maximal width $\geq$ 0.5μm; thin spines were then identified as spines with a length $\geq$ 2.5 spine head mean width, and stubby spines were the remaining spines. For each dendritic stretch, spine density was calculated as ratio relatively to the baseline level, defined as the spine density quantified during the first imaging session. All steps were performed blindly to the experimental conditions.

For expansion microscopy of acute slices or of organotypic slice cultures, z stacks of secondary stretches in the *stratum radiatum* of CA1 pyramidal cells or in the outer molecular layer of dentate granule cells, respectively, were obtained with a two-channel laser-scanning confocal (Leica, TCS SP8) using a 63x water-dipping objective with a 3x zoom. After deconvolution using the CMLE algorithm (automated parameters) of Huygens Professional (Scientific Volume Imaging), the stacks were registered if necessary using a rigid body algorithm using the StackReg plugin (Bioimaging Group, EPFL) in ImageJ (NIH) to correct for lateral movement. Five dendritic stretches per condition per experiment, corresponding to five different neurons and including all visually identified spine types, were selected for further analysis.

A limitation of expansion microscopy is the variability in expansion between samples and within a given sample (anisotropy). While this has been reported especially for fibrous tissues (see e.g., Pernal et al., 2020; Zhao et al., 2017), such anisotropy is highly limited at subcellular compartments, and especially synapses, where expansion microscopy has been shown to generate very low spatial distortion (less than 3%; Jiang et al., 2018; Ku et al., 2016). To prevent any possible bias, we reported AMPAR levels to the volume of each subcellular compartment, and we only compared relative ratios (i.e., surface and internal pools) between samples; we also opted for visual spine identification and classification rather than absolute numerical inputs. The volume of GluA2 and GFP staining in these stretches were reconstructed using the Surface module of Imaris (Bitplane) by a researcher blind to the experimental conditions. To analyze selectively the GluA2 signal pertaining to the dendritic stretch of interest, a mask was created based on the GFP channel with a low intensity threshold to include all GluA2 staining in proximity to that dendritic stretch; all signals not included in this mask (i.e., located far from the dendritic stretch of interest) were hence automatically removed from subsequent analysis. The volumes of the GluA2 and GFP staining were then reconstructed separately and precisely based on the fluorescence intensity with the automatic threshold suggested by Imaris. Reconstructions were carefully compared to the raw data (before deconvolution) to ensure their exactitude. The exact reconstruction of the GFP volume was used as a mask to distinguish between the GluA2 signal within its volume, defined as intracellular GluA2, and GluA2 signal just outside of the GFP reconstruction, defined as surface GluA2, and to separately reconstruct the two pools. The reconstructed GluA2 volume was then quantified and normalized to the volume of the spine head or the shaft as determined by the GFP staining (total GluA2/GFP); the average per spine type/shaft was calculated from all values from that spine type/shaft, and the averages of mushroom, thin, stubby spines and shafts were rescaled to their overall sum to show GluA2/GFP distribution as percentages of total GluA2/GFP. Surface GluA2 was calculated as a percentage of the total GluA2 per spine or shaft, and the average per spine type/shaft was calculated from all individual values. These values were subsequently used for statistical analysis. We also performed staining in non-permeabilizing and permeabilizing conditions followed by expansion microscopy in cultured hippocampal neurons to validate the proxy used (see below). The amount of GluA2 before permeabilization showed the ground truth of GluA2-containing AMPARs at the surface. This amount was similar to the external GluA2 signal at the surface of the GFP staining after permeabilization following the above-mentioned analysis, confirming that the proxy used in OTCs provides a relevant picture of GluA2-containing AMPAR distribution.

For expansion microscopy of hippocampal cultures, z stacks of secondary stretches of GFP-transfected neurons were with a two-channel laser-scanning confocal (Leica, TCS SP8) using a water-dipping 63x objective (3x zoom). Images were deconvolved with Huygens and the GluA2 and GFP stainings were reconstructed using Imaris as described above. For the comparison between the amount of surface GluA2 without permeabilization and after permeabilization (Figure S1E), GluA2 was specifically analyzed at

visually identified mushroom spines. For GluA2 without permeabilization, the amount of GluA2 was quantified by reporting all reconstructed GluA2 volumes to the GFP volume of their corresponding spine and by calculating the average across all spines. For GluA2 after permeabilization, surface GluA2 was defined as described above and all reconstructed volumes were reported to the GFP volume of their corresponding spine; the final value was calculated by averaging all reconstructed surface GluA2 volumes across all spines.

For all representative pictures of expanded data, the scale bars present the physical size of the sample post-expansion, as given directly by the microscope based on the imaging parameters. The original size of the representative pictures is ~3-3.5x smaller, depending on the expansion factor of the corresponding sample. The expansion factor was determined for each sample by measuring the dendritic diameter of several neurons before and after expansion in the same area and by calculating the post- to pre-expansion ratio. For all representative pictures of expanded data except Figures 1A and 1B (top) and S1 B-C, GluA2 staining is shown in two pseudocolors corresponding to the two pools (surface GluA2 (sGluA2) in magenta and internal GluA2 (iGluA2) in cyan) defined using the exact reconstruction of the GFP volume as a mask. For Figures S1B and S1C, magenta is used to show GluA2 staining prior to permeabilization (surface GluA2, sGluA2), while GluA2 staining after permeabilization (total GluA2, tGluA2) is shown in two pseudocolors corresponding to the two pools defined again using the exact reconstruction of the GFP volume as a mask (orange for the surface pool (surface-total GluA2, s-tGluA2) and cyan for the internal pool (internal-total GluA2, i-tGluA2).

QUANTIFICATION AND STATISTICAL ANALYSIS

Statistical analysis was performed on the number of neurons n indicated in the corresponding figure legends, except when showing expanded data, in which case the analysis was done per spine or shaft from 5 neurons. Data are expressed as mean ± standard error of mean (SEM). To assess significance levels, two-way ANOVA (GraphPad, Prism) was used for long-term imaging and the unpaired Student's t test (Excel, Microsoft) for the new AMPAR insertion assay and for baseline spine density. For expansion microscopy, data distribution was assessed using Shapiro-Wilke's normality test; statistical comparisons between datasets that passed the test were performed with the unpaired Student's t test (Excel, Microsoft), while comparisons where at least one dataset that did not pass the normality test were carried out with the corresponding non-parametric test, i.e., the Mann-Whitney-U test (GraphPad, Prism). Representative experiments are shown with either the unpaired Student's t test or Mann-Whitney-U values for that particular experiment; Fisher's combined test was used on all available experiments to verify the reliability of the observed phenotype. Differences were considered significant if $p < 0.05$ and indicated as * if $p < 0.05$, ** if $p < 0.01$ and *** if $p < 0.001$. The exact p values for relations discussed in this manuscript are found in the Table S1.

Cell Reports, Volume *34*

Supplemental information

EphrinB2 and GRIP1 stabilize mushroom spines during denervation-induced homeostatic plasticity

Diane Bissen, Maximilian Ken Kracht, Franziska Foss, Jan Hofmann, and Amparo Acker-Palmer

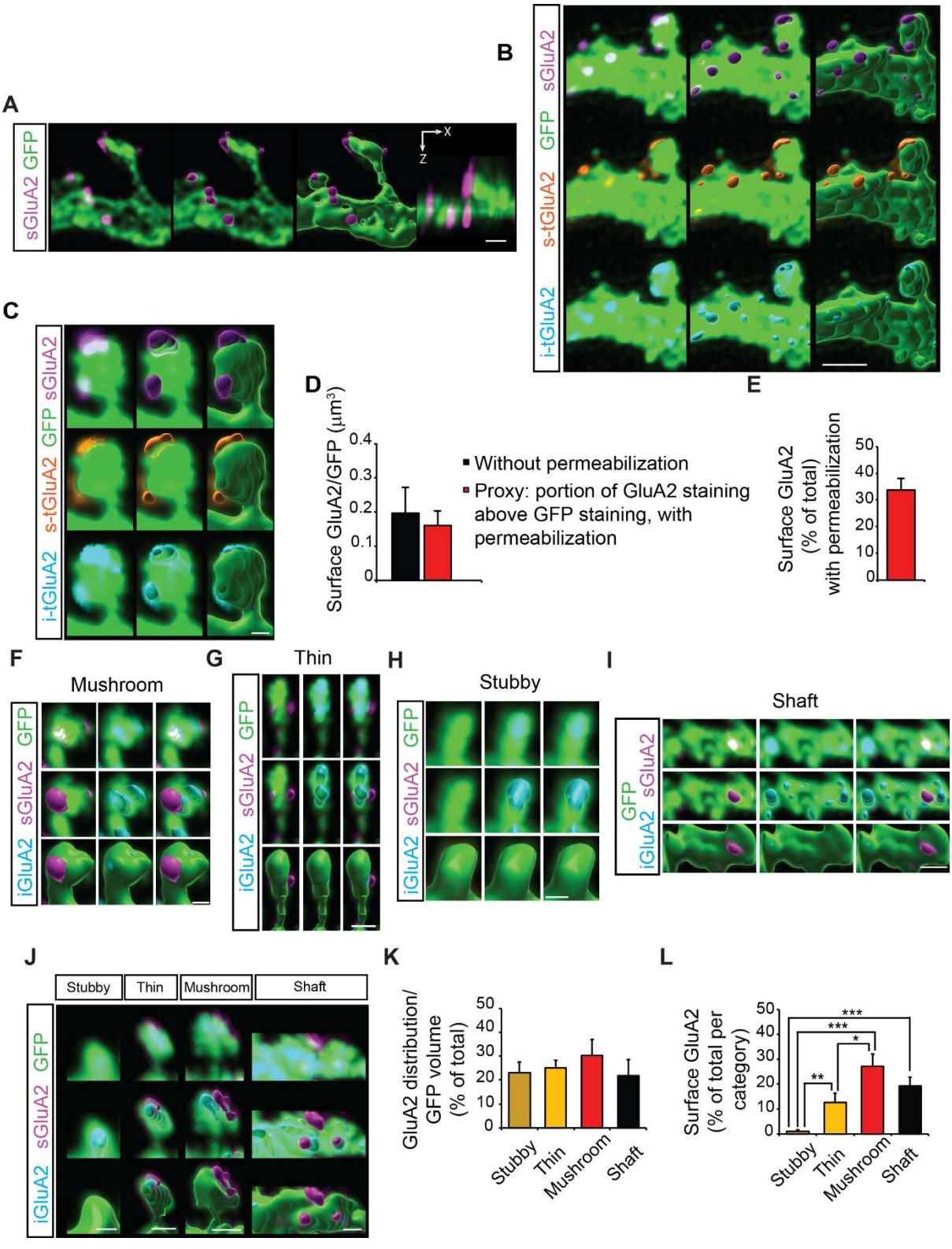
A
sGluA2 GFP
X
Z
B
i-tGluA2
s-tGluA2
GFP
sGluA2
C
i-tGluA2
s-tGluA2
GFP
sGluA2
D
Surface GluA2/GFP (μm³)
0.4
0.3
0.2
0.1
0
Without permeabilization
Proxy: portion of GluA2 staining above GFP staining, with permeabilization
E
Surface GluA2 (% of total) with permeabilization
50
40
30
20
10
0
F
Mushroom
iGluA2
sGluA2
GFP
G
Thin
H
Stubby
I
Shaft
J
Stubby
Thin
Mushroom
Shaft
K
GluA2 distribution/ GFP volume (% of total)
L
Surface GluA2 (% of total per category)
***
***
*
**

Figure S1. Expansion microscopy provides sufficient spatial resolution to discriminate between surface and internal GluA2-containing AMPARs, and AMPAR distribution is similar in CA1 pyramidal cells compared to dentate granule cells. Related to Figure 1.

(A) Representative images from GFP (green) - transfected hippocampal cultures stained for surface GluA2 (sGluA2, magenta) without permeabilization and submitted to expansion microscopy. From left to right: GluA2 and GFP stainings; GluA2 reconstruction and GFP staining; GluA2 and GFP reconstructions. The fourth panel displays GluA2 and GFP staining of the same spine as visible along the Y axis. Scale bar, 1µm.

(B-C) Representative images from GFP (green) - transfected hippocampal cultures stained for surface GluA2 without permeabilization (sGluA2, magenta, top row) and for total GluA2 after permeabilization (tGluA2) using the same antibody; based on the reconstruction of the GFP staining, the latter has been divided between surface GluA2 (s-tGluA2, orange, middle row) and internal GluA2 (i-tGluA2, cyan, bottom row). The left panels show GluA2 and GFP stainings; the middle panels show GluA2 reconstruction and GFP staining; the right panels show both reconstructions. (C) Higher magnification of the mushroom spine in (B). Scale bar, 1µm (B), 0.5µm (C).

(D) Quantification of the amount of GluA2 signal at the surface of mushroom spines, corresponding to (C). For surface GluA2 without permeabilization, the volume of each GluA2 reconstruction was reported to the GFP volume of the corresponding mushroom spine, all volumes were summed per spine, and the average was calculated across all mushroom spines. For total GluA2 after permeabilization, only GluA2 reconstructions at the surface of the GFP volume were considered. Of note, the baseline proportion of surface GluA2 in mushroom spines in hippocampal cultures is statistically similar to what is observed in OTCs under constitutive conditions. Data are shown as mean +/- SEM.

(E) Quantification of surface GluA2 with permeabilization, shown as percentage of total GluA2 (+/- SEM) corresponding to (C).

(F-I) Representative surface reconstructions of the mushroom (F), thin (G), stubby (H) spines and the shaft (I) shown in Fig. 1C. Surface GluA2 (magenta, left column) and internal GluA2 (cyan, middle column) are shown separately and together (right column; as seen in Fig. 1C). From top to bottom: GluA2 and GFP staining; GluA2 reconstruction and GFP staining; GluA2 and GFP reconstruction. Scale bars, 1µm.

(J) Representative surface reconstructions of stubby, thin and mushroom spines and shafts from secondary stretches in the *stratum radiatum* of CA1 pyramidal cells. The surface reconstruction of the GFP staining is not visible in the bottom row to enable visualization of internal GluA2. Scale bars, 1µm.

(K) Quantification of GluA2 distribution normalized to GFP volume, shown as percentage of total GluA2/GFP (+/- SEM) corresponding to (E). n = 5 neurons, 2 experiments.

(L) Quantification of surface GluA2, shown as percentage of total GluA2 per compartment (+/- SEM) corresponding to (E). n = 5 neurons, 2 experiments. *$p < 0.05$, **$p < 0.01$, ***$p < 0.001$.

Exact p-values in Table S1.

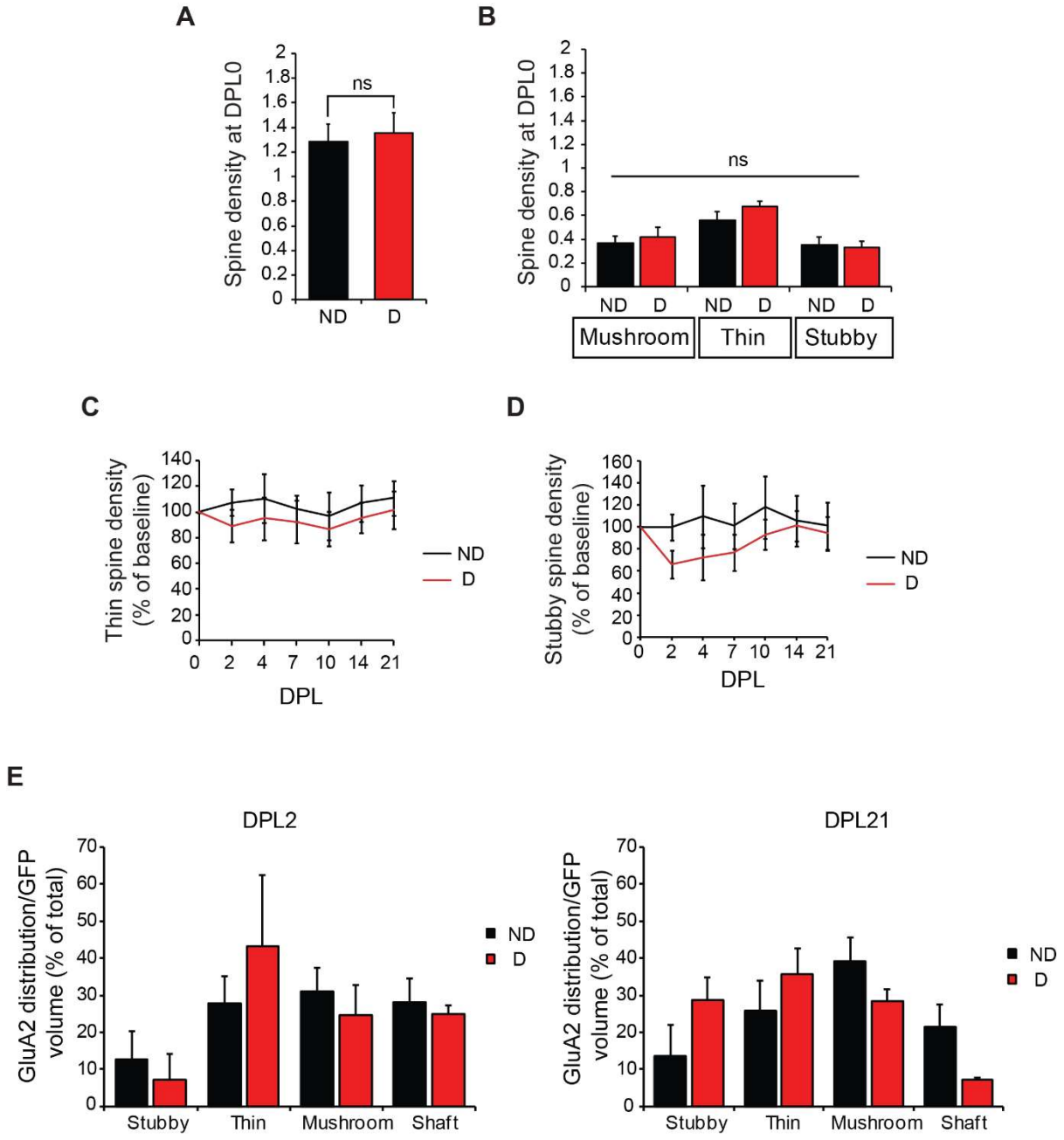

Figure S2. Denervation does not affect thin and stubby spine density nor total AMPAR content. Related to Figure 1.

(A-B) Total spine density (A) and mushroom, thin and stubby spine density (B) at baseline (day post lesion (DPL)0) (+/- SEM) are similar between stretches from OTCs subsequently selected for denervation (D) or as non-denervated controls (ND). ns, not significant.

(C-D) Quantification of thin (C) and stubby (D) spine density in non-denervated and denervated OTCs as relative ratios to baseline (DPL 0) (+/- SEM) corresponding Figure 1 (G). n = 5-7 neurons per condition, 4 experiments.

(E) Quantification of GluA2 distribution normalized to GFP volume at DPL2 and DPL21 in denervated (D) and non-denervated (ND) OTCs (+/- SEM) corresponding to Figure 1 (I-K). n = 5 neurons per condition, 2 experiments.

Exact p-values in Table S1.

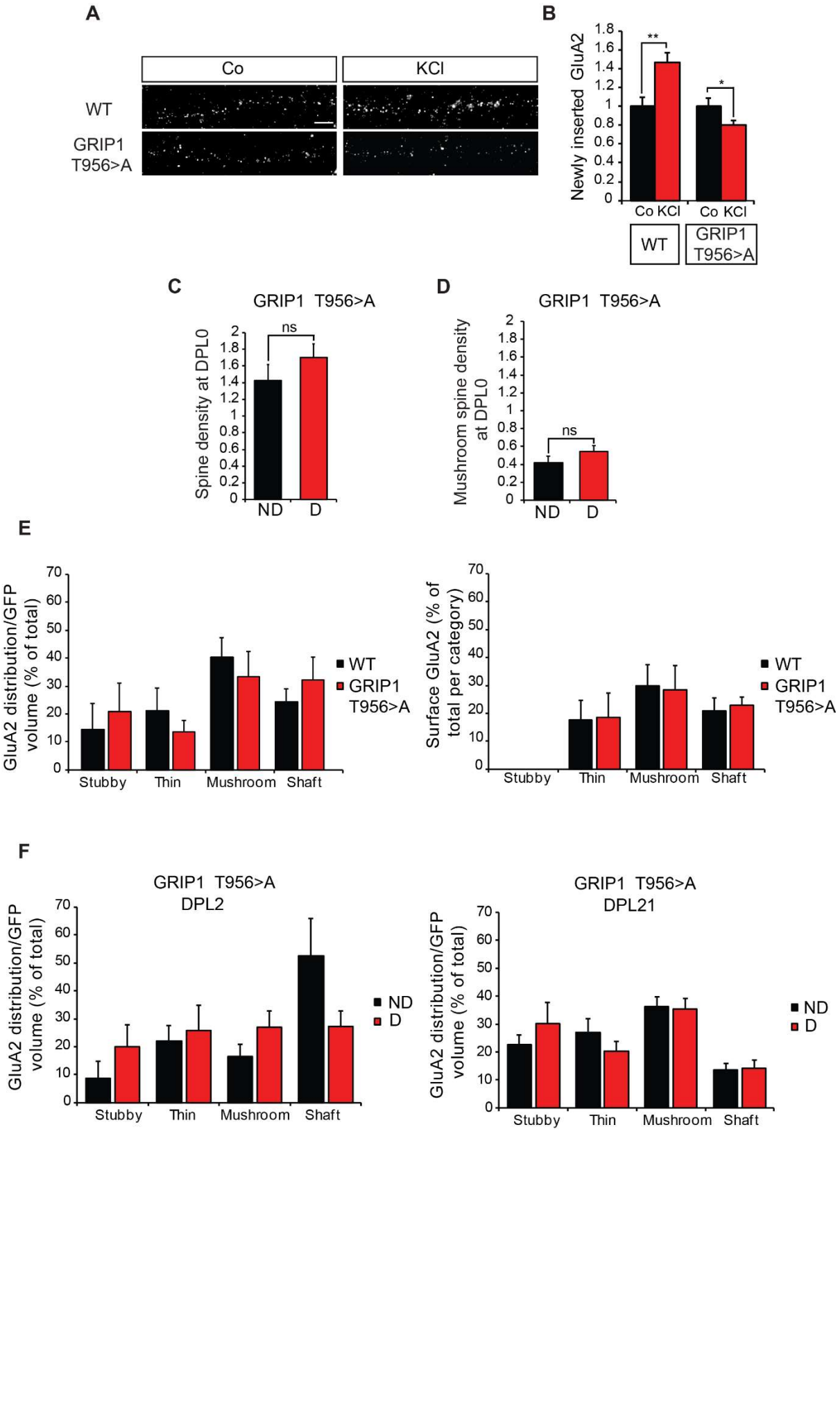
A
Co
KCl
WT
GRIP1
T956>A
B
Newly inserted GluA2
1.8
1.6
1.4
1.2
1
0.8
0.6
0.4
0.2
0
**
*
Co KCl
Co KCl
WT
GRIP1
T956>A
C
GRIP1 T956>A
Spine density at DPL0
ns
ND
D
D
GRIP1 T956>A
Mushroom spine density
at DPL0
ns
ND
D
E
GluA2 distribution/GFP
volume (% of total)
70
60
50
40
30
20
10
0
Stubby
Thin
Mushroom
Shaft
WT
GRIP1
T956>A
Surface GluA2 (% of
total per category)
WT
GRIP1
T956>A
F
GRIP1 T956>A
DPL2
GluA2 distribution/GFP
volume (% of total)
ND
D
GRIP1 T956>A
DPL21
GluA2 distribution/GFP
volume (% of total)
ND
D

Figure S3. T956 phosphorylation is required for GRIP1 function during activity-induced *de novo* AMPA receptor insertion and stabilization, but not for baseline spine density and morphology, nor for AMPAR content and distribution. Related to Figure 2.

(A) Representative pictures of newly inserted GluA2 in dendritic stretches of hippocampal neurons. Scale bar, 5µm.

(B) Quantification of the relative fluorescence intensities (+/- SEM) of the newly inserted GluA2, corresponding to (A). Stimulation is normalized to the control condition. n = 30-60 neurons per condition from 3 experiments. *$p < 0.05$, **$p < 0.01$.

(C-D) Total (C) and mushroom (D) spine density at baseline (DPL0) (+/- SEM) are similar between stretches from *Grip1*-T956>A OTCs subsequently selected for denervation (D) or as non-denervated OTCs (ND). ns, not significant.

(E) Quantification of total GluA2/GFP (left graph) and surface GluA2 (right graph) in non-denervated *Grip1*-T956>A OTCs compared to control (Ctrl) OTCs, (+/- SEM). n = 5 neurons per condition, 2 experiments.

(F) Quantification of total GluA2/GFP distribution at DPL2 and DPL21 in denervated (D) and non-denervated (ND) *Grip1*-T956>A OTCs (+/- SEM). n = 5 neurons per condition, 2 experiments. DPL, Day post lesion.

Exact p-values in Table S1.

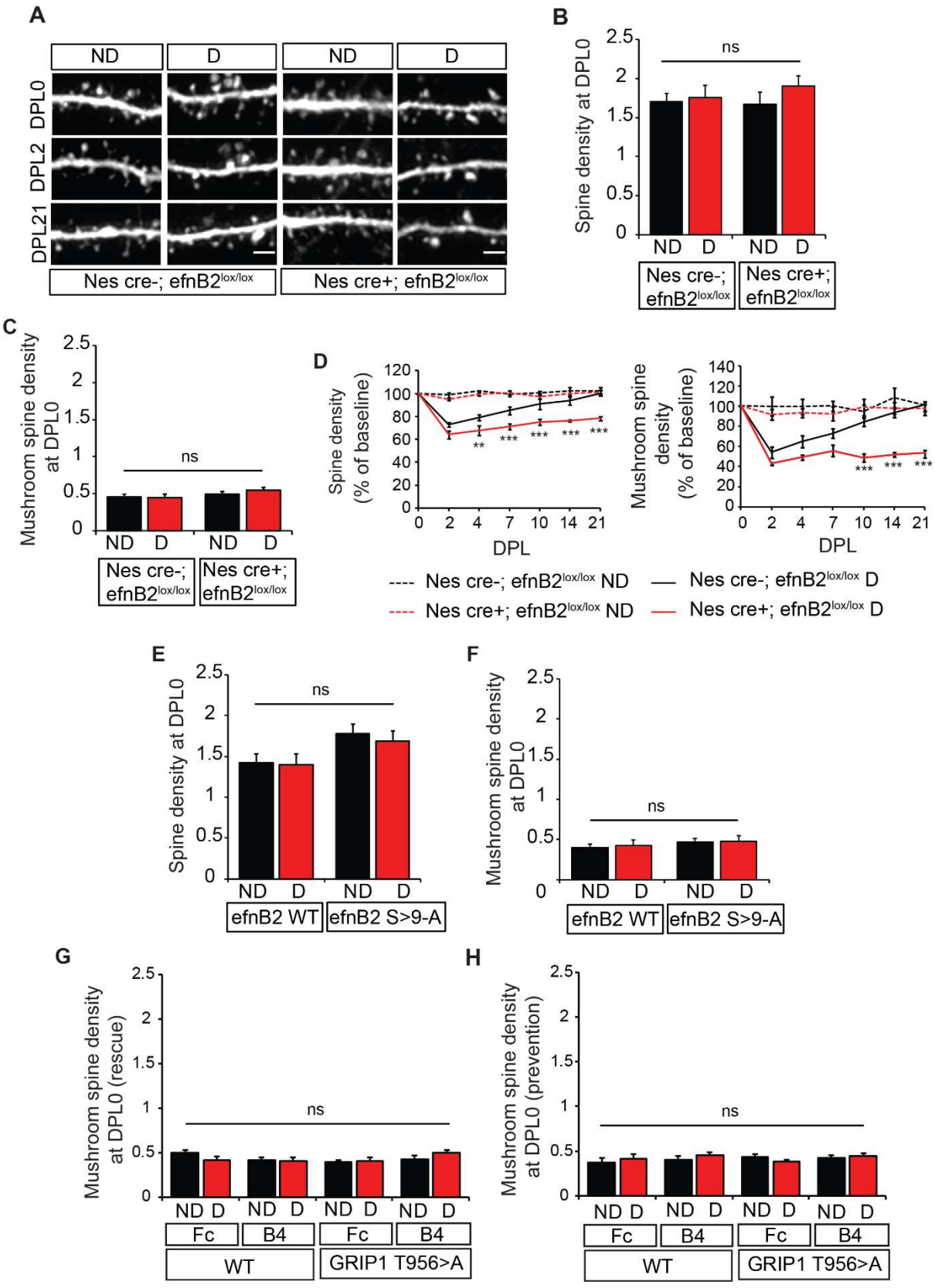
A
ND
D
ND
D
DPL0
DPL2
DPL21
Nes cre-; efnB2lox/lox
Nes cre+; efnB2lox/lox
B
Spine density at DPL0
ns
ND D ND D
Nes cre-; efnB2lox/lox
Nes cre+; efnB2lox/lox
C
Mushroom spine density at DPL0
ns
ND D ND D
Nes cre-; efnB2lox/lox
Nes cre+; efnB2lox/lox
D
Spine density (% of baseline)
DPL
Mushroom spine density (% of baseline)
DPL
Nes cre-; efnB2lox/lox ND
Nes cre-; efnB2lox/lox D
Nes cre+; efnB2lox/lox ND
Nes cre+; efnB2lox/lox D
E
Spine density at DPL0
ns
ND D ND D
efnB2 WT
efnB2 S>9-A
F
Mushroom spine density at DPL0
ns
ND D ND D
efnB2 WT
efnB2 S>9-A
G
Mushroom spine density at DPL0 (rescue)
ns
ND D ND D ND D ND D
Fc
B4
Fc
B4
WT
GRIP1 T956>A
H
Mushroom spine density at DPL0 (prevention)
ns
ND D ND D ND D ND D
Fc
B4
Fc
B4
WT
GRIP1 T956>A

Figure S4. EphrinB2 is crucial for mushroom spine formation and stabilization after lesion-induced loss, but not necessary for baseline spine density and morphology. Related to Figures 3 and 4.

(A) Representative pictures of secondary dendritic stretches of non-denervated and denervated *efnB2* knockout OTCs (*Nes cre+; efnB2*$^{lox/lox}$) and their control littermates (*Nes cre-; efnB2*$^{lox/lox}$) at DPL0, DPL2 and DPL21. DPL, Day post lesion; ND, not denervated; D, denervated. Scale bars, 2µm.

(B-C) Total (B) and mushroom (C) spine density at baseline (DPL0) (+/- SEM) are similar between stretches from *efnB2* knockout or control OTCs subsequently selected for denervation (D) or as non-denervated controls (ND). ns, not significant.

(D) Quantification of total spine (left graph) and mushroom spine (right graph) density at each time point as relative ratios to DPL0 (+/- SEM). Significance levels shown between *Nes cre+; efnB2*$^{lox/lox}$ D and *Nes cre-; efnB2*$^{lox/lox}$ D. n = 6-7 neurons per condition from 3 experiments. **p < 0.01, ***p< 0.001.

(E-F) Total (E) and mushroom (F) spine density at baseline (DPL0) (+/- SEM) are similar between stretches from *efnB2 S-9>A* or control (Ctrl) OTCs subsequently selected for denervation (D) or as non-denervated controls (ND). ns, not significant.

(G-H) Mushroom spine density at baseline (DPL0) (+/- SEM) is similar between stretches from *Grip1*-T956>A or control (Ctrl) OTCs subsequently selected for denervation (D), non-denervation (ND), EphB4-Fc stimulation (B4) or Fc-treatment (Fc) according to the rescue (G) or prevention (H) paradigm. ns, not significant.

Exact p-values in Table S1.